The use of magnetite as a geochemical indicator in the exploration for magmatic Ni-Cu-PGE sulfide deposits: a case study from Munali, Zambia

Laura A. Ward[1], David A. Holwell[1*], Tiffany L. Barry[1], Daryl E. Blanks[1], and Shaun D. Graham[2]

[1]School of Geography, Geology and the Enironment, University of Leicester, University Road, Leicester, LE1 7RH, UK. dah29@le.ac.uk

[2]Carl Zeiss Microscopy Ltd, 509 Coldhams Lane, Cambridge, CB1 3JS, UK

*Corresponding author:

Tel: +44 (0) 116 252 3804

Fax: +44 (0) 116 252 3918

Revision submitted to: Journal of Geochemical Exploration as a Short Communication

Abstract

Magmatic sulfide deposits hosted by mafic-ultramafic intrusions are the most important source of Ni and PGE on Earth. Exploration strategies rely on geophysics to identify the host intrusions, and surface geochemistry to identify anomalous concentrations of Cu, Ni, Co, Cr, As and other associated elements. The use of geochemical indicator minerals in overburden is used widely in diamond exploration and mineral chemistry in fresh rock is increasingly used to identify proxies for mineralisation in magmatic-hydrothermal systems. However, no indicator mineral techniques are routinely applied to magmatic sulfides. Magnetite represents an ideal indicator mineral for this mineralisation style due to its ubiquity in such deposits, its resistance to weathering, its recoverability from soil samples, and its chemical variability under differing conditions of formation. We use the Munali Ni sulfide deposit to test the use of magnetite as an indicator mineral. Magnetite from mafic, ultramafic, and magmatic sulfide lithologies in fresh rock at Munali show discernible differences in the most compatible elements (V, Ni, Cr). We propose a new Cr/V versus Ni discrimination diagram for magnetite that can be used to indicate fractionation of the parent magma (Cr/V increases from ultramafic to mafic), and the presence of co-existing sulfides (Ni contents >300ppm). The signatures of these three elements at Munali are comparable to sulfide-related magnetites from other deposits, supporting the broad applicability of the discrimination diagram. Samples taken from overburden directly on top of the Munali deposit replicate signatures in the fresh bedrock, strongly advocating the use of magnetite as an exploration indicator mineral. Samples from areas without any geophysical or geochemical anomalies show weak mineralisation signatures, whereas magnetite samples taken from prospects with such anomalies display mineralisation signatures. Magnetite is a thus a viable geochemical indicator mineral for magmatic sulfide mineralisation in early stage exploration.

Keywords: Magnetite, LA-ICP-MS, magmatic sulfides, Ni-Cu-PGE, indicator minerals

Introduction

Indicator mineral chemistry has been a successful early stage exploration technique for many years. The key features of successful indicator minerals are that they have a much higher abundance than the main commodity; they survive in weathering processes; and have distinctive geochemical signatures (Layton-Matthews et al. 2014). This approach is well established in diamond exploration, where indicator minerals (e.g. ilmenite, olivine, Cr-diopside, garnet) are present in much higher quantities than diamonds in overburden; and their abundance, co-occurrence and chemistry have been used to identify the presence and fertility of kimberlites (Gurney 1984; Fipke et al. 1995).Early stage geochemical exploration for base and precious metals, conversely, has traditionally relied primarily on bulk elevations of certain elements in overburden and transported (e.g. stream) samples (Cameron and Hattori 2005), alongside geophysical anomalies (Balch 2005). Recently, however, there has been a drive to develop indicator mineral geochemistry for base metal deposits in fresh rock (e.g. Mao et al. 2016); most significantly for porphyry Cu-Au deposits in arc-related magmatic rocks, where plagioclase, apatite, and magnetite have all been shown to be useful in identifying key processes that determine fertility (Williamson et al. 2016; Bouzari et al. 2016; Pisiak et al. 2017).

Magmatic Ni-Cu-platinum group element (PGE) deposits are the world's most important source of Ni and PGEs, accounting for ~56% of the world's Ni production and over 96% of Pt, Pd, and the other PGE production (Mudd and Jowitt 2014). Such deposits are hosted in ultramafic/mafic intrusions that have undergone sulfide saturation and the separation of an immiscible sulfide liquid from the silicate magma, which scavenged chalcophile elements like Ni, Cu, and the PGE (Barnes et al. 2017). Exploration for these deposits has traditionally relied on geophysics; primarily gravity and magnetic surveys to identify the host

ultramafic/mafic complexes; and overburden geochemistry to identify elevated levels of elements like Cu, Ni, Co, As, and Cr (Rose et al. 1979; Cameron and Hattori 2005). Olivine is used as a fresh rock indicator mineral, with its relative enrichment or depletion in Ni content used to indicate sulfide undersaturated, or saturated conditions of formation (e.g., Li and Naldrett 1999), olivine breaks down too easily to be used as an effective indicator mineral in overburden. At present, no minerals are routinely used as indicator minerals in early-stage exploration for magmatic Ni-Cu-PGE sulfides.

Iron-oxides are common accessory minerals across hydrothermal, metamorphic and magmatic ore deposits and magnetite is amongst the most abundant Fe-oxide phase within the continental crust. Magnetite possesses the key properties of a successful indicator mineral, including the ability to incorporate a number of foreign cations (Nadoll et al. 2014), resistance to weathering/erosion, magnetic properties for easy identification and sampling, and it is widespread in many geological settings. Recent advances in the field of Laser Ablation-Inductively Coupled Plasma-Mass Spectrometry (LA-ICP-MS) analysis have been able to further constrain magnetite's petrological significance based on its chemistry (Dupuis and Beaudoin 2011; Nadoll and Koenig 2011; Nadoll et al. 2014; Boutroy et al. 2014; Dare et al. 2014; Chen et al. 2014; Chung et al. 2015; Liu et al. 2015; Zhao and Zhou 2015). Dupuis and Beaudoin (2011) have shown that magnetite formed from different deposit types can be fingerprinted using trace element chemistry and Pisiak et al. (2017) have shown that magnetite chemistry has significant potential to discriminate between mineralised and barren porphyry sources in overburden sampling.

In mafic-ultramafic systems, magnetite can form via fractional crystallisation of a silicate magma, secondary hydrothermal processes (e.g., serpentinisation), or from the fractionation

of Ni-Cu-PGE-bearing sulphide liquids (Dare et al. 2012; 2014; Boutory et al. 2014; Duran et al. 2016). Recent LA-ICP-MS studies of magnetite associated with magmatic Ni-Cu-PGE sulfide has been useful in determining magma and co-existing sulfide compositions, source conditions, fractionation histories and the distinction of magmatic versus hydrothermal origins (Dupuis and Beaudoin 2011; Nadoll et al. 2014; Boutroy et al. 2014; Dare et al. 2014; Liu et al. 2015).

In this paper, we build on this to test the application of magnetite as a geochemical indicator mineral for magmatic Ni-Cu-PGE sulfide mineralisation for the first time. As a case study, we use the Munali Ni sulfide deposit and mine in southern Zambia due to there being: (1) a well characterised multi-stage, magmatic and sulfide history, each with associated magnetite in an economic deposit (Holwell et al. 2017), thus providing a solid framework of local magmatic and mineralised signatures in fresh rock to compare with overburden; (2) topographical and vegetation constraints that limit surface outcrop in places and thus it is an example of where early stage exploration requires surface geochemistry; (3) the presence of a number of prospective locations, based on magnetic (and in some cases surface geochemical) anomalies, that can be used to test whether prospective geochemical signatures in magnetite are replicated proximal to other prospects. Different generations of magnetite are texturally, then geochemically classified, with petrogenesis discussed, and we propose a new discrimination diagram that can become a powerful tool in surface geochemical exploration for Ni-Cu-PGE sulfide deposits.

The Munali Ni sulfide deposit

The mafic-ultramafic Munali Intrusive Complex (MIC) is located in the Zambezi Supracrustal Sequence (ZSS) within the medium-high metamorphic grade Zambezi Belt,

southern Zambia (Evans 2011; Holwell et al. 2017a; Fig. 1A). The ZSS comprises a Neoproterozoic package of metasediments and metavolcanics (Johnson et al. 2007), which defines the east-west striking orogenic belt extending from Central Zambia to northern Zimbabwe (Hanson et al. 1994). During the Neoproterozoic, the southern margins of the Congo Craton were subject to rifting and intraplate magmatism from ~880 to ~820 Ma (Johnson et al. 2007), likely as part of the breakup of the supercontinent Rodinia (John et al. 2003). During this period, magmatism intruded rift sediments that included the multi-stage emplacement of the MIC (862-858 Ma; Holwell et al. 2017a).

The MIC was emplaced along a major NW-SE trending crustal lineament (the Munali Fault, Fig. 1A), proximal to the margins of the southern Congo Craton, into ZSS sediments that comprise marbles, quartzites, and pelites of the Nega Formation (Johnson et al. 2007; Holwell et al. 2017a). Basement material in the Munali Hills region (Fig. 1) comprises the 1106 ± 19 Ma Mpande Gneiss, a complex of gneisses and granites (Hanson et al. 1988), succeeded by the 1090 ± 1.3 Ma Munali Hills Granite (Katongo et al. 2004). The MIC displays a very strong magnetic anomaly, with additional anomalies present along the Munali Fault and the northern fault splay (Fig. 1A), marking the presence of a number of proven and inferred intrusions of a similar genesis (Howe and Holwell. 2016).

The MIC comprises a number of magmatic stages, all of which contain magnetite, but only some also contain magmatic sulfides. The Central Gabbro Unit (CGU), the earliest stage, was emplaced at 862 Ma and does not contain any Ni-sulfide mineralisation. This was followed by the mineralised, Marginal Ultramafic-mafic Breccia Unit (MUBU) emplaced at 858 Ma (Fig. 1; Holwell et al. 2017a). The CGU comprises heterogeneously textured magnetite-bearing gabbro, whereas the MUBU is a chaotic megabreccia unit containing clasts of

poikilitic gabbro, ultramafic olivinites (referred to as such rather than dunites, due to the oxide being magnetite, rather than chromite), olivine-magnetite rocks, phoscorites, and dykes of olivine dolerite, all in a groundmass of sulfide-magnetite-carbonate-apatite (Holwell et al., 2017a). The magmatic sulfide assemblage is pyrrhotite>>pentlandite>chalcopyrite+pyrite and there is evidence of a number of sulfide-magnetite (± carbonate ± apatite) generations within the MUBU (Blanks et al. 2017). Dominant magnetite-bearing rocks at Munali include gabbros of the CGU, poikilitic gabbros, olivinites, and phoscorites of the MUBU, and the dolerite dykes. Magnetite is also present as an essential component within all of the sulfide assemblages: in the massive breccia fill and late stage sulfide-carbonate veins of the MUBU,.

Materials and methods

Twelve samples of quarter core were selected from a suite of samples from diamond drill holes that intercepted the MUBU and CGU of the MIC, comprising a range of representative magnetite styles. All drillcores sampled were drilled through the southern MUBU in the MIC (Fig. 1B). Five detrital magnetite samples (OB01-05) were collected from the soil overburden on top of the MIC, and proximal to other regional magnetic/geochemical anomalies (Fig. 1B). Locations of soil samples are shown in Figure 1B. Magnetite from soil samples was separated using a magnet and mounted in resin and made into polished blocks. All size fractions were retained from this method, and the size of grains ranged up to 500 µm.

Mineralogical, petrological, and textural analysis of oxides and associated sulphides was undertaken on twelve polished thin sections and five mounted detrital magnetite samples. Second generation automated mineralogy was conducted at ZEISS' Natural Resources Laboratory in Cambridge, UK. Mineralogic Mining software was used to quantitatively classify mineralogy, major element chemistry, and magnetite textures. The technique maps

the samples and quantifies EDS spectra allowing quantitative phase identification and element deportment (Holwell et al. 2017b). Spot analyses were undertaken to be used for LA-ICP-MS normalisation. Full analytical conditions and methodology is detailed in Supplementary Material A1.

Magnetite in all samples was then subject to LA-ICP-MS analysis. The methodology and list of trace elements analysed was conducted in accordance to recent studies of LA-ICP-MS performed on magnetite (e.g., Dare et al. 2014; Boutroy et al. 2014). A natural magnetite standard from the Bushveld Complex (BC-28) provided by S-J. Barnes (Université de Québec à Chicoutimi, Canada) was used to monitor data quality and ensure internal data consistency. Laser Ablation-ICP-MS was conducted at the University of Leicester using a New Wave Research-ESI 213 nm laser coupled with a ThermoScientific iCAP-Qc quadrupole ICP mass spectrometer. Full analytical conditions and methodology are detailed in Supplementary Material A1.

Petrology and classification of magnetite styles

The mineralogical mapping of thin sections allowed full textural and petrological classification of a number of magnetite styles. These can split into four textural categories: (1) igneous magnetite in mafic and ultramafic rocks; and in syn-MUBU dolerite dykes; (2) magnetite related to massive sulfides that forms the matrix in the MUBU; (3) magnetite formed as reaction rinds; and (4) late stage magnetite in carbonate-sulfide injections and veins in the MUBU. The textural characteristics described below are summarised in Table 1.

Igneous magnetite in mafic/ultramafic rocks

This textural category comprises magnetite that is considered a normal rock-forming constituent. All of the magnetite of this style that we analysed can be considered Ti-poor,

containing <1 wt% Ti based on EDX analysis. The CGU, and the poikilitic gabbro clasts in the MUBU, are mineralogically similar, though differ texturally (Fig. 2A,B), comprising a silicate assemblage of plagioclase and clinopyroxene with up to 20 modal % magnetite and lesser ilmenite. The finer-grained CGU can be characterised by interstitial grains of magnetite (Fig. 2A). Very minor pyrrhotite is present (Fig. 2Aii), but there is no appreciable Ni-Cu-PGE mineralisation and these rocks are considered unmineralised, or barren in this sense. In the poikilitic gabbro, magnetite is present as large oikocrysts (<20 mm) with accompanying plagioclase chadacrysts (Fig. 2B). No inclusions (sulfide or otherwise), were observed within magnetite in either the CGU or the poikilitic gabbro, though both contain abundant ilmenite occurring as two textures: (1) coarse-grained ilmenite blebs intergrown with magnetite (Fig. 2Aiii, 2Bii); and, (2) fine laths of exsolved ilmenite commonly in trellis patterns (Fig. 2Aiii, 2Bii). The poikilitic gabbro contains a minor primary sulphide assemblage (<1% modal mineralogy; pyrrhotite>>pentlandite>chalcopyrite; Fig. 2Bi), and thus is considered to be weakly mineralised.

Magnetite is a ubiquitous and often abundant constituent of the ultramafic rocks of the MUBU (Fig. 2C). Olivinites grade into olivine-magnetite rocks and phoscorites (olivine-magnetite-apatite) and contain large cumulus olivine crystals up to several centimetres in diameter, and interstitial magnetite and apatite. Magnetite is present as large sub-angular grains (<1 cm) containing frequent ilmenite lamellae (Fig. 2Cii). Nickel-Cu sulfides are sporadic, but occur as large interstitial blebs in textural equilibrium with interstitial magnetite and apatite (Fig. 2C) and as such these rocks are considered mineralised.

The latest intrusive stage is the emplacement of dolerite dykes, which comprise a silicate assemblage of plagioclase with actinolite pseudomorphs of clinopyroxene phenocrysts and

totally altered and serpentinised olivine phenocrysts (Fig. 2D). Minor, disseminated magnetite is present in addition to coarser magnetite grains (<3 mm) occurring in textural equilibrium with ilmenite in equal abundance (Fig. 2Dii). Very minor pyrrhotite is present (Fig 2Dii), but these are considered, like the CGU, to be barren of Ni-Cu-PGE mineralisation.

Magnetite within massive sulfide assemblages

Magnetite is always present within pyrrhotite-pentlandite-chalcopyrite-pyrite blebs and accumulations, comprising typically ~5, but up to 20, modal %, of the sulfide assemblage that makes up the breccia matrix of the MUBU. Magnetite is spatially associated with massive sulphide, and as such, is believed to have formed via the direct fractionation of a sulphide liquid (Fig. 3A). Whilst texturally associated with sulphide, it is important to note that some magnetite in this association may in fact be xenocrysts from mafic-ultramafic phases disaggregated during brecciation (c.f. Fig. 13D of Holwell et al. 2017a). Magnetite is present as large (<1.5 cm) sub-angular grains that exhibit no preference to any single sulfide mineral (Fig. 3A).

Magnetite in late stage carbonate-sulfide veins

Carbonate-associated magnetite is present intergrown with primary calcite and dolomite and sulfide in late stage veins/injections within the MUBU (Fig. 3B). Sub-angular magnetite grains marginal to sulphide are common, though less abundant than sulphide, making up ~5 modal % of the mineralogy. Generally, ilmenite is uncommon though the largest magnetite grains (<3 mm) exhibit minor ilmenite association (Fig. 3Bii).

Reaction rind magnetite

Reaction-rind magnetite can be divided into two subcategories based on adjacent material: (1) at sulphide-silicate boundaries, often seen around the margins of sulphide-enclosed mafic and

ultramafic xenoliths within the MUBU and at the boundary between massive and semi-massive sulfide veins and mafic/ultramafic host rocks (Fig. 3C); and (2) silicate-silicate reaction rinds between mafic lithologies, predominantly between poikilitic gabbro and dolerite intrusions (Fig. 3D). The sulphide-silicate reaction rinds are the more dominant of the two sub-categories, typically forming 1-2 cm thick rims made up of 100% magnetite against adjacent silicate rocks (Fig. 3C). Rinds form irrespective of silicate rock composition. Silicate-silicate magnetite reaction rinds comprise 1-1.5 cm thick rims (Fig. 3D). Magnetite tends to exhibit a euhedral morphology (Fig. 3D) defining the contact between the silicate rocks.

Magnetite geochemistry

Laser-Ablation-ICP-MS data is reported for all textural magnetite styles. Full LA-ICP-MS datasets can be found in Supplementary Material A2. Multi-element plots (Fig. 4) have been devised for the four textural magnetite classifications and lithological subdivisions for elements above detection (Si, Y, Pb, Zr, Hf, Al, Ge, W, Sc, Ta, Nb, Cu, Sn, Ga, Mg, Ti, Zn, Co, V, Ni and Cr). Elements are plotted in order of compatibility into magnetite (left to right; Dare et al., 2014). The LA-ICP-MS data shown in Figure 4 has been normalised to the composition of bulk continental crust (Rudnick and Gao 2003) to compare the compositions of source magmas (Dare et al. 2012; Boutroy et al. 2014). Figure 5 illustrates a time-resolved analysis (TRA) profile for a typical laser track across a composite magnetite-ilmenite grain to clearly illustrate the elements that are relatively enriched in magnetite (Fe, Cr, V, Co, Ni, and Ga; Fig 5A), compared to ilmenite (Ti, Al, Ta, Y, W, Cu, Nb, Pb; Fig 5B). Whilst every effort was made to only include parts of each analysis that ablated magnetite, some ilmenite will have been homogenised into the LA data (this is seen in the LA-ICP-MS data indicating up to 10 wt% Ti, whereas the EDS analysis gave a maximum of 1 wt%). As such, variations

in each of the plots shown in Figure 4 in the latter set of elements are likely due to variable contents of ilmenite included. This is seen in the variation in Ti (ilmenite controlled) in Fig. 4C versus Ga (magnetite controlled).

Magnetite is variably enriched in Sn, Ga, Mg, Ti, Co, V, Ni, and Cr relative to bulk continental crust in most styles (Fig. 4), whereas Si, Y, Pb, Zr, Hf, Ta, Nb, and Cu are relatively depleted, which is expected given their relative incompatibility into magnetite. The concentration of highly compatible elements in magnetite (Cr, Ti, and V) across all styles are typically an order of magnitude higher than incompatible elements (e.g., Si, Y, Pb, and Zr). Chromium, an element commonly enriched in mafic-ultramafic systems, is remarkably depleted at Munali and no chromite is found within the ultramafic rocks (Holwell et al. 2017a). However, the Cr concentrations in magnetite from the MIC (60-2600 ppm) are not significantly lower than those reported for magnetite in other mafic-ultramafic intrusions (e.g., 24-5668 ppm; Dare et al. 2012).

Igneous magnetite in mafic/ultramafic rocks

The geochemical profiles for all the analysed igneous magnetites are comparable, with some notable exceptions that distinguish some of the separate phases. For example, the poikilitic gabbro demonstrates Cr enrichments and Y and Ta depletions compared to the rest of the Munali mafic rocks (Fig. 4A). The dolerite dykes have the lowest Zn concentrations of any of the mafic rocks. Chromium concentrations are higher in mafic lithologies (<505 ppm) than in ultramafic rocks (<72 ppm). Both the mafic and ultramafic magnetites at Munali demonstrate variable enrichment in Al, Sc, Sn, Ga, Mg, Ti, Zn, Co, V, Ni, and Cr, with element abundances consistently higher in mafic relative to ultramafic rocks (Fig. 4). The sulfide-bearing poikilitic gabbro has higher Ni contents than the sulfide-poor mafic lithologies (~10x

and ~2x bulk continental crust, respectively), higher Cr and lower V, and lower Ta and Nb contents (Fig. 4A).

Magnetite within massive sulfide assemblage

All magnetite analysed that was associated with massive sulfides (Fig. 3A) share geochemical similarities, suggestive of a common origin, though they display subtle differences in Zr, Hf, Ta, Zn, W, Cu, and Cr (Fig. 4C) and exhibit the highest Cr values of any style (up to 3132 ppm). Notably, magnetite in igneous rocks that contain sulfides (poikilitic gabbro, ultramafics) share similar profiles with magnetite in massive sulfides that make up the matrix of the MUBU; most notably with consistent Ni contents around 10 times higher than bulk continental crust (~600 ppm). Furthermore, whilst of different generations, both the poikilitic gabbro and the ultramafic rocks contain interstitial sulfides, yet magnetite chemistry is comparable between these. Thus chemically, all magnetite associated with either massive sulfide, or rocks containing disseminated sulfide show similar characteristics. Therefore, irrespective of generation, there appears to be a common signature, which reflects the co-existence of sulfides. There are, however, some clear differences in the overall profile with a notable depletion in Ta-Nb in massive sulfide-associated magnetite relative to the igneous phase magnetite (Fig. 4C), with the exception of the sulfide-bearing poikilitic gabbro.

Magnetite in late stage carbonate-sulfide veins/injections

Similarities are observed between magnetite in carbonate-sulfide veins and those from the massive sulfides. Geochemical profiles of magnetite in the sulfide-carbonate veins are comparable with those in the massive sulfides (Fig. 4C) and poikilitic gabbro (Fig. 4A);

sharing similar enrichments in Ni. The carbonate-associated magnetites differ slightly from the massive sulfide magnetites in having higher Nb, and lower Cr contents (Fig. 4C).

Reaction rind magnetite

There are some significant differences between the two textural sub-classifications of reaction rinds, with sulfide-silicate reaction rinds notably more enriched in Zr, Hf, Sc, Cu, Mg, Zn, and Cr compared to silicate-silicate rinds (Fig 4D). Overall, the geochemical profiles are distinct not just from each other, but from both the igneous phase magnetite and sulfide-associated magnetite; however, the sulfide-silicate reaction rind magnetite shares a similar V-Ni-Cr signature to the massive sulfides.

Cr/V versus Ni discrimination diagram for magnetite

Although it has been shown that late stage hydrothermal re-equilibration of hydrothermal magnetite can modify textures and compositions (Hu et al., 2014; 2015), the most compatible elements in magnetite (e.g., V, Cr, Ni, and Co) are relatively immobile (Hu et al., 2014), and thus the contents and ratios of these elements can be a very robust indicator of provenance, unaffected by hydrothermal overprints.

Chromium, V, and Ni have been selected for use as discriminant criteria for the following reasons: (1) good degrees of data reliability; (2) they are compatible in magnetite with limited influence by ilmenite crystallisation (Fig. 5), and also have minimal mobility during hydrothermal alteration (Hu et al., 2014); (3) they show clear differences in profiles between different textural types that reflect lithology and/or the presence of sulfide (Fig. 4); and (4) Ni is a useful element in tracing sulfide-saturation of a magma. Using these elements, we propose a new discrimination diagram that can be used in exploration as a way of

distinguishing magnetite from different lithologies and those associated with sulfide mineralisation (Fig. 6).

The ratio between Cr and V concentrations is an efficient lithological discriminant, dividing igneous textural types into two distinct geochemical fields, with Cr/V in ultramafic rocks <0.022. Alone however, Cr/V ratios are ineffective in distinguishing magnetite in mineralised and barren rocks, but Ni shows a clear cut off at 300 ppm; with all magnetite above this in rocks with magmatic sulfides, the reasons for which will be discussed later. Therefore we present plots of Cr/V versus Ni (Fig. 6) where three *geochemical* (c.f. textural) classifications can be recognised:

1. High Ni and Cr/V ore-related magnetite (including: poikilitic gabbro from the igneous phase textural association; magnetite associated with massive sulfide; and magnetite associated with carbonate-sulfide);
2. High Ni and low Cr/V ultramafic magnetite (including all ultramafic rocks in the igneous phase textural class); and
3. Low Ni and high Cr/V barren igneous phase magnetite (including all non-mineralised mafic rocks from the igneous phase textural class; and the silicate-silicate reaction rind textural classification).

The silicate-silicate reaction rind samples sit within the barren igneous field on the Ni diagram (Fig. 6), but the sulfide-silicate reaction rinds sit very close to the boundary of barren and mineralised and are the closest group to the ore-related field, with a relatively high Cr/V ratio as well (Fig. 6).

Detrital magnetite petrology and geochemistry

Detrital magnetite was sampled from overburden above the Munali deposit, and three other areas within the Munali Hills region (Fig. 1B). Figure 7 illustrates some of the typical morphologies and sizes of the detrital grains recovered from overburden in these areas. In samples taken from the northeastern part of the study area (OB1-3), the grains typically have a subrounded morphology and are somewhat pitted (Fig. 7A,B) compared with those taken directly above the MIC, which are more angular (Fig. 7C,D); most likely reflective of the transport distance from their source. Irrespective of the shape, ilmenite exsolution lamellae are preserved (e.g., Fig. 7B). Figure 7D shows the track of the laser during a typical line analysis over one such grain (c.f. Fig. 5).

As both mineralised and barren magnetite geochemical signatures for the main magnetite-bearing bedrock lithologies at Munali have been established, detrital magnetite can be compared using the Cr/V versus Ni discriminant diagram (Fig. 8). Magnetite collected from soil directly on top of the MUBU in the MIC (OB04; Fig. 8A) displays Cr-V-Ni relationships almost identical to the mineralised fields from the primary rocks. This is critical as these data demonstrate that:

1. Magnetite sampled directly on top of known sources of economic grade mineralisation preserves mineralised signatures;
2. Magnetite chemistry of the original host rock is preserved in detrital grains; and
3. Cr, V, and Ni are sufficiently immobile to efficiently preserve the chemistry of known source origins.

A second sample taken from soil over the MIC (OB05; Fig. 8B) shows a wider spread in compositions, but most of the grains overlap with the fields from the fresh rocks. An exception is the four grains that have Cr/V ratios consistent with the ultramafic rocks, but contain ‘barren’ levels of Ni. In fact, none of the detrital grains match the ultramafic

signature in terms of Ni content, but many plot in the low Cr/V ultramafic field with ‘barren’ Ni signatures. This may indicate Ni is somewhat mobile during weathering and that these grains may have experienced more weathering/transport from their source. As such, the 300 ppm Ni cut-off in bedrock may be lowered slightly with the degree of weathering.

One other sample returned magnetite compositions consistent with a Munali sulfide signature. Sample OB01 was collected close to the Termite prospect, a large magnetic anomaly on the southern edge of a soil and termite mound geochemical anomaly (Figs. 1A, 8C). This sample exhibited two clear populations: one that overlaps the Munali mineralised field very closely; and one that displays a linear trend with low Ni and mafic Cr/V ratios. The former indicates that magnetite in the Termite area has signatures of mineralisation, analogous to Munali; the significance of which is discussed below. The latter indicates the presence of another generation of magnetite that is either not present, or was not sampled, in the MIC.

Two samples were taken from along strike from Munali, with OB02 (Fig. 8D) taken from an area with no magnetic or geochemical anomaly, and OB03 (Fig. 8E) taken from above the Chibuku magnetic anomaly. Both samples show evidence of the linear low-Ni population, and also a few points that plot above the ‘mineralised’ Ni concentration (Fig. 8D,E), though in terms of the proportion of overall grains, there are fewer mineralisation indicators than the other three samples. Chibuku is a mafic-ultramafic intrusion with indications of mineralisation potential from Cu/Pd ratios (Howe and Holwell 2016), that does not crop out, but is proven to be present at ~200 m depth from a single exploration drillhole. It would not be expected that any indicator minerals would be present from an intrusion present at such

depth, although given the very limited drilling, some parts of it may be closer to the surface, which may be a source for the mineralised signatures in the overburden.

Discussion

The Munali area provides an excellent test ground to assess the applicability of magnetite as an indicator mineral. Firstly, there are a number of generations of magnetite that are abundant in the MIC, which have discernible geochemical characteristics; most importantly, between magnetite associated with sulfides, and those in barren rocks. Secondly, the Ni, Cr, and V concentrations of magnetite can be used to identify such signatures in soil effectively. The following discussion firstly briefly addresses the processes that determine the variability in magnetite chemistry at Munali, and then focusses on the application of this to exploration.

Origin of different styles and chemical signatures of magnetite

There are three separate origins of the magmatic magnetite in our study: (1) that formed from the fractional crystallisation of a silicate liquid; (2) that formed from the crystallisation of a sulfide melt; and (3) that formed during silicate-silicate or –sulfide interaction. Each of these has distinct geochemical signatures indicative of the different modes and conditions of formation as would be expected (Dupuis and Beaudoin 2011; Nadoll et al. 2014; Boutroy et al. 2014; Dare et al. 2011, 2014).

Dare et al. (2014) showed that the relationship between Ti and Ni/Cr ratio in magnetite could be used to distinguish a magmatic or hydrothermal origin. Our data, plotted on a Ni/Cr versus Ti plot, together with the fields of Dare et al. (2014) in Figure 9A, shows that magnetite in all but the ultramafic magnetites plot in the magmatic field. The textural evidence is clearly in favour of a magmatic origin for the ultramafics (Fig. 2) and the high Ni/Cr ratio reflects the

low Cr and high Ni content of the ultramafic (phoscoritic) magnetites (Fig. 4B), and is not necessarily an indicator of a hydrothermal origin. Phoscorites contain low levels of Cr (<82 ppm), and magnetites from other phoscorites have typically low Cr and Ni (<0.02 wt% of oxides) and high MgO (2.5-8 wt%) and Al_2O_3 (0.5-3.8 wt%) contents (Krasnova et al. 2004). The magnetite from the ultramafics we have analysed contain on average 70 ppm Cr, 2.2 wt% MgO, and 2.2 wt% Al_2O_3. The exception is the Ni content in the Munali ultramafic magnetites is high. Phoscorites rarely contain appreciable magmatic sulfides, so the presence of Ni-sulfides co-existing with the magnetite may account for the high Ni contents (see below). The amount of fractionation of a silicate magma affects the V content of magnetite, with early, more primitive magnetite being more enriched in V (Dare et al. 2014). Thus, the Cr/V ratio can be used as proxy for fractionation and this is seen by the difference between the more primitive ultramafic (lower Cr/V) and more evolved mafic (higher Cr/V) rocks in Figure 6.

Up to 30% magnetite can crystallise directly from a sulphide liquid (Naldrett 1969; Fonseca et al. 2008; Boutroy et al. 2014). All lithophile elements are compatible into Fe-oxide as a result of their relative incompatibility into sulphide (Dare et al. 2011; Boutroy et al. 2014) and thus are concentrated in the oxide, and excluded from the sulfide on cooling. The concentration of chalcophile elements in magnetite, however, is responsive to co-crystallising sulphide (Dare et al. 2014). As such, although genetically the igneous phase and sulfide-associated magnetites differ in terms of texture and lithophile contents, the chalcophile contents of both textural styles are affected by the presence of sulfide. This is seen in the consistent Ni relationships in sulfide-bearing and sulfide-barren samples (Fig. 6).

Copper concentrations within magnetite have been suggested as a proxy for sulphide mineralisation (e.g., Dare et al. 2014), as Cu, along with other chalcophile elements, including Ni, should be concentrated into the sulfide liquid, thus being depleted in any co-existing phase (analogous to Ni depletion in olivine formed from a sulfide-saturated magma; Li and Naldrett 1999). Whilst the ilmenite effect on Cu analysis precludes any rigorous testing of this on magnetite, it is interesting to note that whilst magnetites in massive sulfides have some of the lowest Cu contents (Fig 4). The expected depletion of Ni in sulfide-associated magnetite does not occur and requires some explanation. We suggest that enriched Ni contents in magnetites formed from the fractionation of a sulfide liquid may be the result of initial concentration of Ni into the sulfide liquid, which attains Ni concentrations in the wt % range, rather than, for comparison, a few hundreds of ppm in a silicate melt. The subsequent formation of magnetite from a Ni-enriched sulfide liquid as opposed to a Ni-poor silicate liquid produces magnetite with relatively higher Ni contents (though still with the overwhelming bulk of Ni partitioning into sulfide). Thus the enrichment in Ni in magnetite over Cu is effectively a measure of the $D_{\text{sulfide/magnetite}}$ during sulfide-magnetite crystallisation. Essentially, Cu and Ni will partition into sulfide liquid, but as that fractionates to Ni-rich monosulfide solid solution (mss), Cu-rich intermediate solid solution (iss), and magnetite, virtually all the Cu will stay in sulfide, but some Ni will partition into the magnetite formed in this way. Importantly, this feature means that *elevated Ni* signatures in magnetite indicate co-existing magmatic sulfide formation, and Cu is an unrealiable measure of the presence of sulfide.

The origin of the reaction rinds between the massive sulfides and silicate clasts within the MUBU was discussed by Holwell et al. (2017a), who proposed they were analogous to chromite reaction-rinds observed in komatiite-hosted sulphide deposits formed by

disequilibrium between sulfide and silicate melts (Groves et al. 1977; Dowling et al. 2004). At Munali, this process formed magnetite rather than chromite in the absence of appreciable Cr (Holwell et al. 2017a). The sulfide-silicate reaction rind compositions sit neatly midway between the ore-related and barren mafic fields on the Cr/V versus Ni plot (Fig. 6) and thus conceivably represent signatures inherited from a mixture of sulfide and silicate sources. Silicate-silicate rinds are most commonly observed between dolerite and poikilitic gabbro, and have compositions that sit within the barren mafic field and thus reflect the mafic nature of the two rock types they separate.

The detrital grains in our study also show at least one chemically distinct population of magnetite that do not have a magmatic equivalent within the Munali system. Whilst these could be sourced from a distinct magmatic event that is not present within the MIC, it is pertinent to explore the possibility that these grains have a very different source. Firstly, it has been established that magnetite can undergo significant dissolution and reprecipitation (DRP) processes under hydrothermal conditions (Hu et al. 2015). There is obvious rounding and pitting in some of the detrital grains we studied (Fig. 7A,B), but this is most likely due to mechanical weathering and erosion. The high temperature oxy-exsolution of ilmenite lamellae are preserved in the detrital grains (Fig. 7B), but there is perhaps some evidence of the secondary textural generations of magnetite observed as characteristic of DRP (Fig. 7B; c.f. Hu et al. 2015).

The Ni-poor geochemical population (Fig. 8) are present in samples in the northwest of the study (samples OB1-3; Fig 8C-D) and are characterised by extremely low Ni contents (<30 ppm) and a positive correlation between Ni and Cr/V ratio (Fig. 8). Hydrothermal magnetite from both skarns and Late Proterozoic ironstones have been recorded to have Ni contents

typically around 10, and Cr/V ratios <1 (Zhao and Zhou, 2015; Chung et al. 2015); consistent with the low-Ni population in Figure 8C-E. Therefore, we suggest that to the northwest of Munali, there is likely to be a bedrock source of hydrothermal magnetite, and that grains sourced from this may have undergone some DRP (Fig. 7B).

Application to exploration

Magnetite is a ubiquitous accessory mineral in magmatic sulfide assemblages and a common igneous phase in many related mafic rocks, with distinctive chemistries due to different conditions of formation. It is resistant to weathering and is easily recovered during overburden sampling due to its magnetic properties. As such, it has great potential to be used as an indicator mineral in exploration. Our study demonstrates three critical relationships that provide proof of concept for the use of magnetite as a geochemical indicator mineral in early stage exploration for Ni-Cu-PGE sulfide deposits.

1. The Cr/V versus Ni discrimination diagram provides a powerful tool for determining magnetite formed from mineralised and barren systems;
2. The comparison shown in Figure 9 illustrates how Cr, V, and Ni at our case study area is consistent with other deposits worldwide. Thus, our discrimination diagram is widely applicable; and
3. The transfer of geochemical signatures from bedrock sources into overburden shows that using the Cr/V versus Ni discrimination diagram for soil samples is robust and the signatures are representative of the source.

Dupuis and Beaudoin (2011) showed that Cr+Ni versus Si+Mg discrimination diagrams can effectively discriminate magnetite formed in different ore deposit types; distinguishing Ni-Cu-PGE deposits from a range of other magmatic and hydrothermal deposit types. Where our

study advances this is in the proposal of the Cr/V versus Ni discrimination diagram that can discriminate fractionation effects and the co-existence of sulfides *within* this environment.

Both Cu and Ni have the potential to be discriminators of sulfide saturated and undersaturated rocks. However, there are problems with using Cu, related to its compatability in ilmenite (Fig. 5). Co-crystallising ilmenite will render the surrounding magnetite Ti-poor (Nadoll et al. 2014) and thus the relative amount of co-existing ilmenite will control the Cu content of the magnetite, which presents a restricting factor in the use of Cu as a proxy for mineralisation. We conclude that Ni is more reliable due to: (1) the higher compatability of Ni in magnetite resulting in its presence in concentrations comfortably above detection limits; (2) Ti-rich magnetite and ilmenite are more likely to incorporate Cu than Ti-poor magnetite, potentially introducing a biasing component, especially in analysis of magnetite with ilmenite exsolution lamella; and (3) Cu is a more mobile element in the surficial environment and can thus be remobilised during weathering. That said, there is some evidence from the lack of ultramafic signatures with Ni >300 ppm in the overburden at Munali (Fig 7B) that may indicate some loss of Ni in the surficial environment.

Our work has some specific implications for the prospectivity of the Munali Hills region. The fewer number of grains with mineralised signatures from soil samples in the centre of the study area is consistent with no evidence of major intrusions close to the surface in those areas. However, the Termite prospect has magnetite in soil that has Cr-V-Ni signatures indicative of magmatic sulfide mineralisation. As such, coupled with the known Cu and Ni soil geochemical and magnetic anomalies in this area, this would be consistent with a significant indication of magmatic sulfide mineralisation at Termite. This illustrates how

magnetite indicator mineral chemistry within a soil sampling program can add further confidence to early stage prospectivity and fertility assessments.

The determination of mineralised/barren and mafic/ultramafic fields on the Cr/V versus Ni discrimination diagram we present is based on the ability to define the fields with available bedrock material. It would always be optimal to have a control on the likely local signatures, however, in greenfields exploration areas, this may not be possible. Our discrimination quadrants are based on the signatures present in the case study area we used, and are necessarily restricted by any particular local signatures. The sulfide composition at Munali is consistent with most Ni-sulfide deposits, and is an Fe-rich, mss-like orebody (Holwell et al. 2017a). Magnetite associated with mineralisation at Munali is plotted onto diagrams devised by Boutroy et al. (2014) to assess the composition of the sulphide liquid (Fig. 9B,C). This confirms that magnetite associated with the main sulphides at Munali is consistent with the chemical signature of Fe-rich, as opposed to Cu-rich sulfides (Holwell et al. 2017a). It also implies that the interstitial sulfides in the ultramafic rocks (which are temporally earlier) are slightly more evolved; consistent with a multi-stage history in the MIC (Holwell et al. 2017a).

One of the most significant conclusions to be drawn from the relationship shown in Figure 9B,C is that the Cr, Ni, and V contents of the sulfide-associated Munali magnetite are similar to those from other sulfide deposits. This means that the fields in the Cr/V versus Ni discrimination diagram should be widely applicable to any magmatic sulfide deposit. Given that hydrothermal magnetite generally has very low Ni contents (Zhao and Zhou, 2015; Chung et al., 2015), we would suggest that any analyses plotting below around 30 ppm Ni may be considered to have a likely hydrothermal origin as discussed above. However, use of

the Ti v Ni/Cr discrimination diagram proposed by Dare et al. (2014) is an effective determinant of hydrothermal versus magmatic origins, and the key application of our Cr/V versus Ni diagram is to identify mineralised magmatic signatures.

It is worth noting that some Ni-Cu-PGE reef deposits are hosted within cumulates where chromite is the oxide present, and not magnetite, and the Merensky Reef, Platreef and UG2 PGE deposits in the Bushveld Complex, for example, do not contain any cumulus magnetite (Naldrett et al. 2011; McDonald and Holwell 2011). However, magnetite is a ubiquitous (though often minor) component of magmatic sulfide assemblages, and therefore whilst in some cases, the Cr/V distinction for lithologies may be not be applicable due to the lack of igneous phase magnetite, the presence of Ni-enriched magnetite derived from sulfide assemblages (for which the sulfide will have degraded during weathering) can still be used as an effective indicator for mineralisation.

Summary

One of the greatest challenges in exploration is the recognition of mineralisation at greater and greater distances from the primary source (Nadoll et al. 2014). Our proof of concept study clearly shows the potential to use magnetite as a geochemical indicator mineral in surface sampling to identify magmatic Ni-Cu-PGE sulfide mineralisation. We have shown this to be effective directly above and within at least ~1 km of magnetic anomalies/surface outcrops, however, there are various parameters not considered in this work, including, though not exclusive to, prevailing wind directions, heterogeneous weathering regimes, surface water flow directions and the potential for bidirectional transport of magnetite grains away from the primary source. Further development of the application of magnetite to early stage exploration will necessarily need to consider these factors. Nevertheless, magnetite can

be considered to be an ideal indicator mineral for magmatic sulfide fertility in that it is abundant, chemically variable, with distinctive signatures related to the presence, or absence, of sulfides.

Acknowledgments

The management and staff of Consolidated Nickel Mines and Mabiza Resources, in particular Simon Purkiss and Matthew Banda, are thanked for logistical and financial support for LAW's MGeol project work. Assistance in the field from Danny Musemeka, Chloe Mitchell and Grace Howe are acknowledged. Carl Zeiss Microscopy is acknowledged for access to Mineralogic Mining software and SEM analysis and both technical and financial support of LAW's MGeol project. Reviews by two anonymous referees and suggestions from Associate Editor David Lentz are gratefully acknowledged for improving the quality of the manuscript.

REFERENCES

Balch S (2005) The geophysical signatures of PGE deposits. In: Mungall JE (ed) Exploration for platinum-group element deposits, Min Ass Canada Short Course Series 35:275-285

Barnes SJ, Holwell DA, LeVaillant ML (2017) Magmatic sulfide ore deposits. Elements 13;91-97

Blanks DE, Holwell DA, Barnes SJ (2017) Magmatic sulphide mineralisation of the Munali nickel deposit: evidence for immiscible sulphide-carbonate-phosphate- silicate melts? Proceedings of the 14th SGA Biennial Meeting, 20-23 August 2017, Québec City, Canada, 415-418

Boutroy E, Dare SA, Beaudoin G, Barnes S-J, Lightfoot PC (2014) Magnetite composition in Ni-Cu-PGE deposits worldwide: application to mineral exploration. J Geochem Expl 145:64-81

Bouzari F, Hart CJR, Bissig T, Barker S (2016) Hydrothermal alteration revealed by apatite luminescence and chemistry: a potential mineral for exploring covered porphyry copper deposits. Econ Geol 111: 1397-1410

Cameron EM, Hattori KH (2005) PGE in geochemical exploration. In: Mungall JE (ed) Exploration for platinum-group element deposits. Min Ass Canada Short Course Series 35:287-307

Dare SA, Barnes S-J, Beaudoin G (2012) Variation in trace element content of magnetite crystallized from a fractionating sulfide liquid, Sudbury, Canada: implications for provenance discrimination. Geochim Cosmochim Acta 88:27-50

Dare SA, Barnes SJ, Beaudoin G, Méric J, Boutroy E, Potvin-Doucet C (2014) Trace elements in magnetite as petrogenetic indicators. Mineral Deposita 49:785-796

Dowling SE, Barnes SJ, Hill RET, Hicks JD (2004) Komatiites and nickel sulfide ores of the Black Swan area, Yilgarn Craton, Western Australia. 2: Geology and genesis of the orebodies. Mineral Deposita 39:707-728

Dupuis C, Beaudoin G (2011) Discriminant diagrams for iron-oxide trace element fingerprinting of mineral deposit types. Miner Deposita 46:319–335

Duran CJ, Barnes S-J, Corkery JT (2016) Trace element distribution in primary sulfides and Fe–Ti oxides from the sulfide-rich pods of the Lac des Iles Pd deposits, Western Ontario, Canada: Constraints on processes controlling the composition of the ore and the use of pentlandite compositions in exploration. J Geochem Explo 166:45-63

Evans DM (2005) Geology and geochemistry of Munali Nickel Deposit: consulting report. Carrog Consulting 34pp

Evans DM (2011) Geodynamic setting of Neoproterozoic nickel sulphide deposits in eastern Africa: Appl Earth Sci (Trans Inst Mining Metall B) 120:175-186

Fipke CE, Gurney JJ, Moore RO (1995) Diamond exploration techniques emphasising indicator mineral chemistry and Canadian examples. Geol Surv Canada Bull 423

Fonseca ROC, Campbell AH, O'Neill HSC, Fitzgerald JD (2008) Oxygen solubility and speciation in sulphide-rich mattes. Geochim Cosmochim Acta 72:2619–2635

Groves DI, Barrett FM, Binns RA, McQueen KG (1977) Spinel phases associated with metamorphosed volcanic-type iron-nickel sulfide ores from Western Australia. Econ Geol, 72:1224–1244

Gurney JJ (1984) A correlation between garnets and diamonds in kimberlites. In: Glover JE and Harris PG (eds) Kimberlite occurrence and origin: a basis for conceptual models in exploration, 8, Univ Western Aus, Perth, W Aus 143-166

Hanson RE; Wilson TJ, Wardlaw MS (1988) Deformed batholiths in the Pan-African Zambezi belt, Zambia: age and implications for regional Proterozoic tectonics. Geology 16:1134–1137

Hanson RE, Wilson TJ, Munyanyiwa H (1994) Geologic evolution of the Neoproterozoic Zambezi orogenic belt in Zambia. J Afr Earth Sci 18:135–150

Holwell DA, Mitchell CL, Howe GA, Evans DM, Ward LA, Friedman R (2017a) The Munali Ni sulfide deposit, southern Zambia: A multi-stage, mafic-ultramafic, magmatic sulfide-magnetite-apatite-carbonate megabreccia. Ore Geol Rev 90:553-575

Holwell DA, Adeyemi Z, Ward LA, Smith DJ, Graham SD, McDonald I, Smith JA (2017b) Low temperature alteration of magmatic Ni-Cu-PGE sulfides as a source for hydrothermal Ni and PGE ores: a quantitative approach using automated mineralogy. Ore Geol Revs 91:718-740

Howe GA, Holwell DA (2016) Assessment of the Ni-Cu-PGE sulphide potential of magmatic intrusions surrounding the Munali Ni-sulphide deposit, Zambia. Appl Earth Sci (Trans Inst Mining Metall B) 125:85

Hu H, Duan Z, Luo Y, Li J-W (2014) Trace element systematics of magnetite from the Chengchao iron deposit in the Daye district: A laser ablation ICP-MS study and insights into ore genesis. Acta Petrol Sinica 30:1292-1306

Hu H, Li J-W, Lentz D, Ren Z, Zhao X-F, Deng X-D, Hall D (2014) Dissolution-reprecipitation process of the magnetite from the Chengchao iron deposit: insights into ore genesis and implications for in-situ chemical analysis of magnetite. Ore Geol Rev 57:393-405

Hu H, Lentz D, Li J-W, McCarron T, Zhao X-F and Hall, D (2015) Reequilibration processes in magnetite from iron skarn deposits. Econ Geol 110:1-8

John T, Schenk V, Haase K, Scherer E, Tembo F (2003) Evidence for a Neoproterozoic ocean in south-central Africa from mid-oceanic-ridge–type geochemical signatures and pressure temperature estimates of Zambian eclogites. Geology 31:243-246

Johnson S, De Waele B, Evans D, Banda W, Tembo F, Milton J, Tani K (2007) Geochronology of the Zambezi Supracrustal sequence, southern Zambia: a record of Neoproterozoic divergent processes along the southern margin of the Congo Craton. J Geology 115:355-374

Katongo C, Kolker F, Klotzli U, Koeberl C, Tembo F, De Waele B (2004) Petrography, geochemistry and geochronology of granitoid rocks in the Neoproterozoic- Paleozoic Lufilian-Zambezi belt, Zambia: implications for tectonic setting and regional correlation. J. Afr. Earth Sci 40:219–244

Krasnova NI, Petrov TG, Balaganskaya EG, Garcia D, Moutte J, Zaitsev AN, Wall F (2004) Introduction to phoscorites: occurrence, composition, nomenclature and petrogenesis. In: Wall F, Zaitsev AN (Eds) Phoscorites and Carbonatites from Mantle to Mine: the Key Example of the Kola Alkaline Province. Mineral Soc Great Britain and Ireland, London 43-72

Layton-Matthews D, Hamilton C, McClengahan MB (2014) Mineral chemistry: modern techniques and applications to exploration. In: McClenaghan MB, Plouffe A, Layton-Matthews D (Eds) Application of Indicator Mineral Methods to Mineral Exploration. Geol Surv Canada, Open File 7553:9–18

Li C, Naldrett AJ (1999) Geology and petrology of the Voisey's Bay intrusion: reaction of olivine with sulfide and silicate liquids. Lithos 47:1-31

Mao M, Rukhlov AS, Rowins SM, Spence J, Coogan LA (2016) Apatite trace element compositions: a robust new tool for mineral exploration. Econ Geol 111:1187-1222

McDonald I, Holwell DA (2011) Geology of the northern Bushvled Complex and the setting and genesis of the Platreef Ni-Cu-PGE deposit. Revs Econ Geol 7:297-328

Mudd GM, Jowitt SM (2014) A detailed assessment of global nickel resource trends and endowments. Econ Geol 109:1813-1841

Nadoll P, Koenig AE (2011) LA-ICP-MS of magnetite: methods and reference materials. J Anal At Spectrom 26:1872-1877

Nadoll P, Angerer T, Mauk JL, French D, Walshe J (2014) The chemistry of hydrothermal magnetite: a review. Ore Geol Rev 61:1–32

Naldrett AJ (1969) A portion of the Fe–O–S system between 900 and 1080°C and its application to sulfide ore magma. J. Petrol 10:171–201

Naldrett AJ, Kinnaird JA, Wilson A, Yudovskaya M, Chunnet G (2011) Genesis of the PGE-enriched Merensky Reef and chromitite seams of the Bushveld Complex. Revs Econ Geol 17:235-296

Pisiak LK, Canil D, Lacourse T, Plouffe A, Ferbey T (2017) Magnetite as an Indicator Mineral in the Exploration of Porphyry Deposits: A Case Study in Till near the Mount Polley Cu-Au Deposit, British Columbia, Canada. Econ Geol 112:919-940

Rudnick RL, Gao S (2003) Composition of the continental crust. Treatise on geochemistry 3:659pp

Williamson BJ, Herrington RJ, Morris A (2016) Porphyry copper enrichment linked to excess aluminium in plagioclase. Nature Geosci 9:237-241

Figure captions

Fig 1 A: Regional gravity map of the Munali area showing the major crustal lineaments of the NW-SE Munali Fault, and its WNW-ESE northern splay; along with several magnetic anomalies located along them, including the Munali Intrusive Complex (MIC), the Chibuku intrusion and the Termite prospect (modified from Evans 2005). Inset: location of Munali within Zambia. B: geological map of the Munali Hills area showing the location of the MIC and the five soil samples (OB01-05) used in this pilot study. Grid system is in UTM, projection WGS84.

Fig 2 Textural association of magnetite in igneous rocks of the MIC illustrated through Mineralogic phase mapping, backscattered SEM imaging and thin section transmitted light. A: Central Gabbro Unit microgabbro: (i) Mineralogic colour coded oxides and sulfides on transmitted light image; (ii, iv) Mineralogic phase map on transmitted light image showing magnetite-ilmenite textures and very minor pyrrhotite; (iii) backscattered SEM image showing magnetite-ilmenite textures. B: poikilitic gabbro: (i) Mineralogic colour coded oxides and sulfides on transmitted light image; (ii) backscattered SEM image showing magnetite-ilmenite textures; (iii) transmitted light image showing magnetite oikocryst with plagioclase chadocrysts. C: coarse grained ultramafic phoscorite with interstitial sulfide-oxide-apatite blebs: (i) Mineralogic colour coded oxides, apatite, sulfides and zircon on transmitted light image; (ii) backscattered SEM image of magnetite-ilmenite textures with included zircon; (iii) transmitted light image showing magnetite in association with apatite in serpentinised olivine. D: olivine dolerite dyke: (i, iii) Mineralogic colour coded oxides and sulfides on transmitted light image; (ii) Mineralogic phase map showing magnetite-ilmenite textures and very minor pyrrhotite. Abbreviations: mt=magnetite, ilm=ilmenite, po=pyrrhotite, pn=pentlandite, plag=plagioclase, ol=olivine.

Fig 3 Textural association of magnetite in MUBU sulfide rocks, and as reaction rims in the MIC illustrated through Mineralogic phase mapping, backscattered SEM imaging and thin section transmitted light. A: typical massive sulfide with magnetite: (i,ii,iv) Mineralogic phase maps showing

pyrrotite-pentlandite loop textures, minor chalcopyrite and large magnetite-ilmenite blebs; (iii) backscattered SEM image of magnetite-ilmenite texture. B: sulfide-carbonate-magnetite vein: (i,ii,iv) Mineralogic phase map of sulfides and oxides on transmitted light image showing sulfide oxide textures with euhedral carbonate crystals; (iii) backscattered SEM image of magnetite-ilmenite texture. C: core sample showing magnetite reaction rind between semi-massive sulfide and adjacent CGU gabbro. D: transmitted light image of magnetite reaction rind between dolerite and poikilitic gabbro. Abbreviations: mt=magnetite, ilm=ilmenite, po=pyrrhotite, pn=pentlandite, cpy=chalcopyrite, py=pyrite, cal=calcite.

Fig 4 Bulk continental crust-normalised multi-element plots from LA-ICP-MS of magnetite (normalisation values from Rudnick and Gao 2003). A: Magnetite from mafic igneous rocks; B: magnetite from ultramafic rocks; C: magnetite from sulfide-dominant lithologies in the MUBU; D: magnetite in reaction rinds.

Fig 5 Time resolved analysis (TRA) spectra of a single laser traverse across magnetite (mt) and ilmenite (ilm). A: response of elements compatible in magnetite; and conversely B: response of elements compatible in ilmenite.

Fig 6 Plot of Cr/V versus Ni for all magnetite analyses from the MIC, defining four discriminating fields based on fractionation (Cr/V) and the presence of sulfide (Ni).

Fig 7 Reflected light photmicrographs of detrital magnetite grains mounted in resin showing (A-C) - variable morphology. A: pitted and rounded morphology from erosion and transport from a sample away from any outcropping igneous rocks; B: rounded grain with ilmenite exsolution lamellae; C: relatively fresh and angular grain from soil directly above the Voyager gossan at Munali, reflective of little transport. D: the track of the laser ablation analysis in a typical line anaysis across a magnetite grain that

Fig 8 Detrital magnetite chemistry of soil samples from the Munali Hills area plotted on Cr/V versus Ni discrimination diagram. Fields are from the Munali bedrock samples shown in Figure 6, and are: UM = ultramafic; M = mafic; and S = sulfide-bearing. Grid system is in UTM, projection WGS84.

Fig 9 Comparison of the MIC magnetite with other discriminant fields. A: all MIC magnetite plotted on the Ni/Cr versus Ti magmatic-hydrothermal discrimination diagram of Dare et al. (2014); B and C: All sulfide-bearing MIC magnetite plotted on the Cr versus V and Ni sulfide evolution discrimination diagrams of Boutroy et al. (2014).

Table 1. Summary of the textural classifications of magnetite in bedrock samples from Munali.

Textural classification	Host rock	Modal abundance magnetite	Associated mineralogy	Sulfide abundance	Textural characteristic
Igneous rocks					
CGU	gabbro	<20%	plagioclase, clinopyroxene	none	oikocrystic magnetite with ilmenite
Poikilitic gabbro	gabbro	<20%	plagioclase, clinopyroxene	very minor	oikocrystic magnetite with ilmenite
Ultramafic	phoscorites, olivinites	<50%	olivine, apatite	sporadic	interstitial magnetite with apatite and sulfide
Olivine dolerite	fine grained basalt/dolerite	<2%	altered plagioclase, clinopyroxene, minor olivine	none	disseminated magnetite
Syn-brecciation MUBU sulfides					
MUBU sulfides	massive sulfide	<20%	pyrrhotite, pentlandite, chalcopyrite	major	magnetite part of fractionated sulfide blebs/patches
Late stage MUBU sulfides					
MUBU sulfide-carbonate	carbonate-sulfide veins	5%	dolomite, calcite, sulfides	major	magnetite part of fractionated sulfide blebs/patches
Reaction rinds					
Sulfide-silicate	sulfide-gabbro/ultramafic, massive sulfide	<100%	n/a	in adjacent rock	massive magnetite rind ~1 cm
Silicate-silicate	dolerite-gabbro	<100%	n/a	none	massive magnetite rind ~1 cm

Supplementary material A1: SEM and LA-ICP-MS methodology

Supplementary material A2: Table A2. LA-ICP-MS data of magnetite from the MIC and overburden samples.

Fig 1

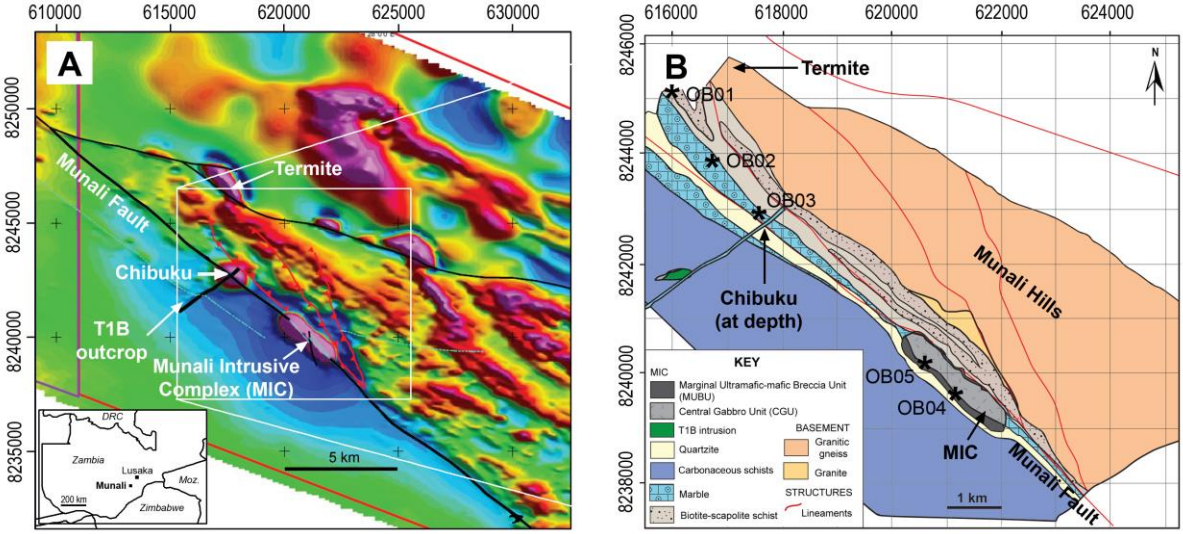
A
610000
615000
620000
625000
630000
8250000
8245000
8240000
8235000
Termite
Munali Fault
Chibuku
T1B
outcrop
Munali Intrusive
Complex (MIC)
5 km
DRC
Zambia
Lusaka
Munali
Moz.
Zimbabwe
200 km
B
616000
618000
620000
622000
624000
8246000
8244000
8242000
8240000
8238000
Termite
OB01
OB02
OB03
Chibuku
(at depth)
Munali Hills
OB05
OB04
MIC
Munali Fault
1 km
N
KEY
MIC
Marginal Ultramafic-mafic Breccia Unit (MUBU)
Central Gabbro Unit (CGU)
T1B intrusion
Quartzite
Carbonaceous schists
Marble
Biotite-scapolite schist
BASEMENT
Granitic gneiss
Granite
STRUCTURES
Lineaments

Fig 2

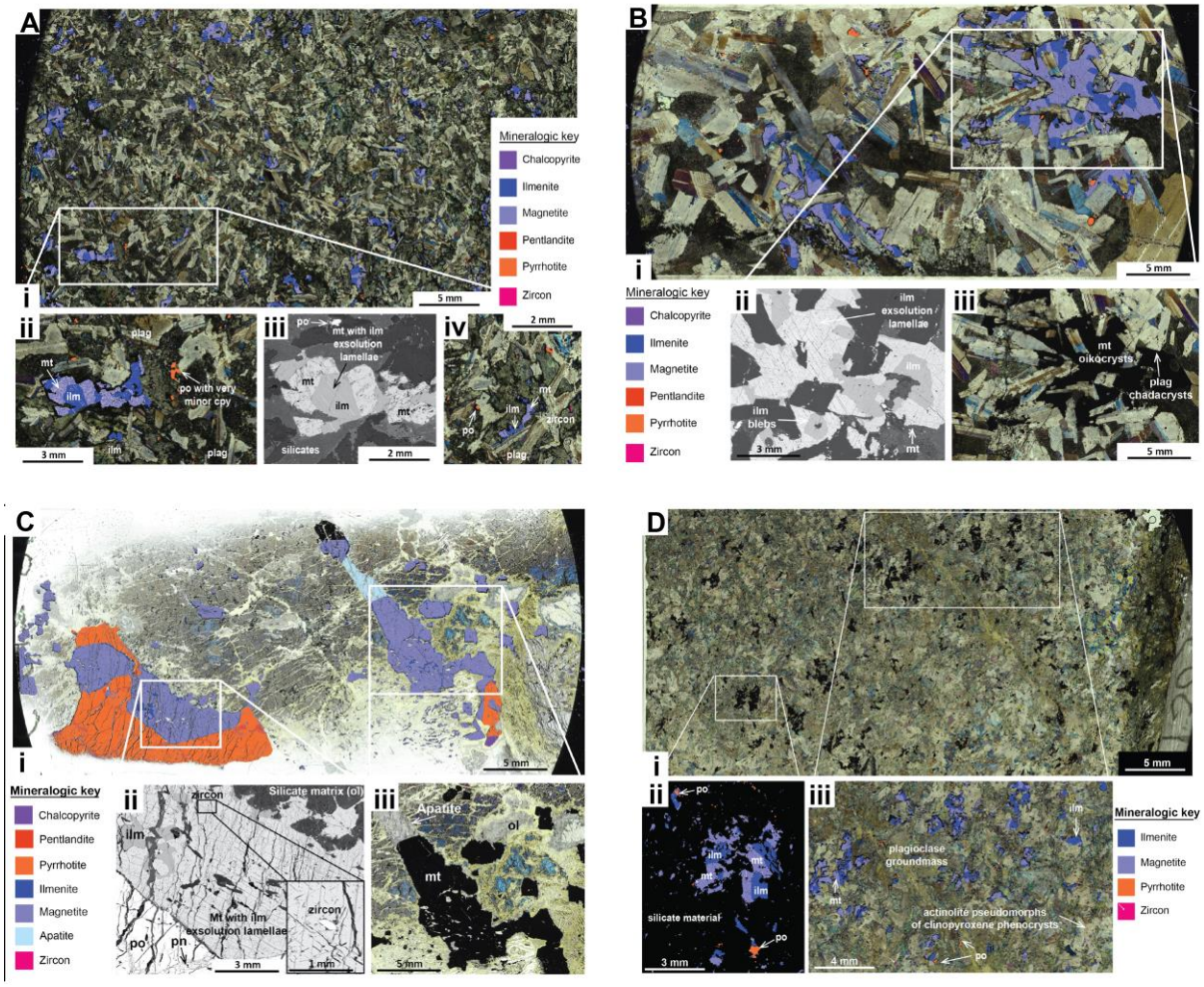
A
Mineralogic key
Chalcopyrite
Ilmenite
Magnetite
Pentlandite
Pyrrhotite
Zircon
5 mm
i
ii
plag
mt
ilm
po with very minor cpy
3 mm
iii
po
mt with ilm exsolution lamellae
silicates
2 mm
iv
2 mm
B
5 mm
i
ii
ilm exsolution lamellae
ilm blebs
3 mm
iii
mt oikocrysts
plag chadacrysts
5 mm
C
5 mm
i
ii
zircon
Silicate matrix (ol)
ilm
Mt with ilm exsolution lamellae
po
pn
3 mm
1 mm
iii
Apatite
ol
mt
5 mm
D
5 mm
i
ii
po
ilm
mt
silicate material
3 mm
iii
ilm
plagioclase groundmass
actinolite pseudomorphs of clinopyroxene phenocrysts
4 mm

Fig 3

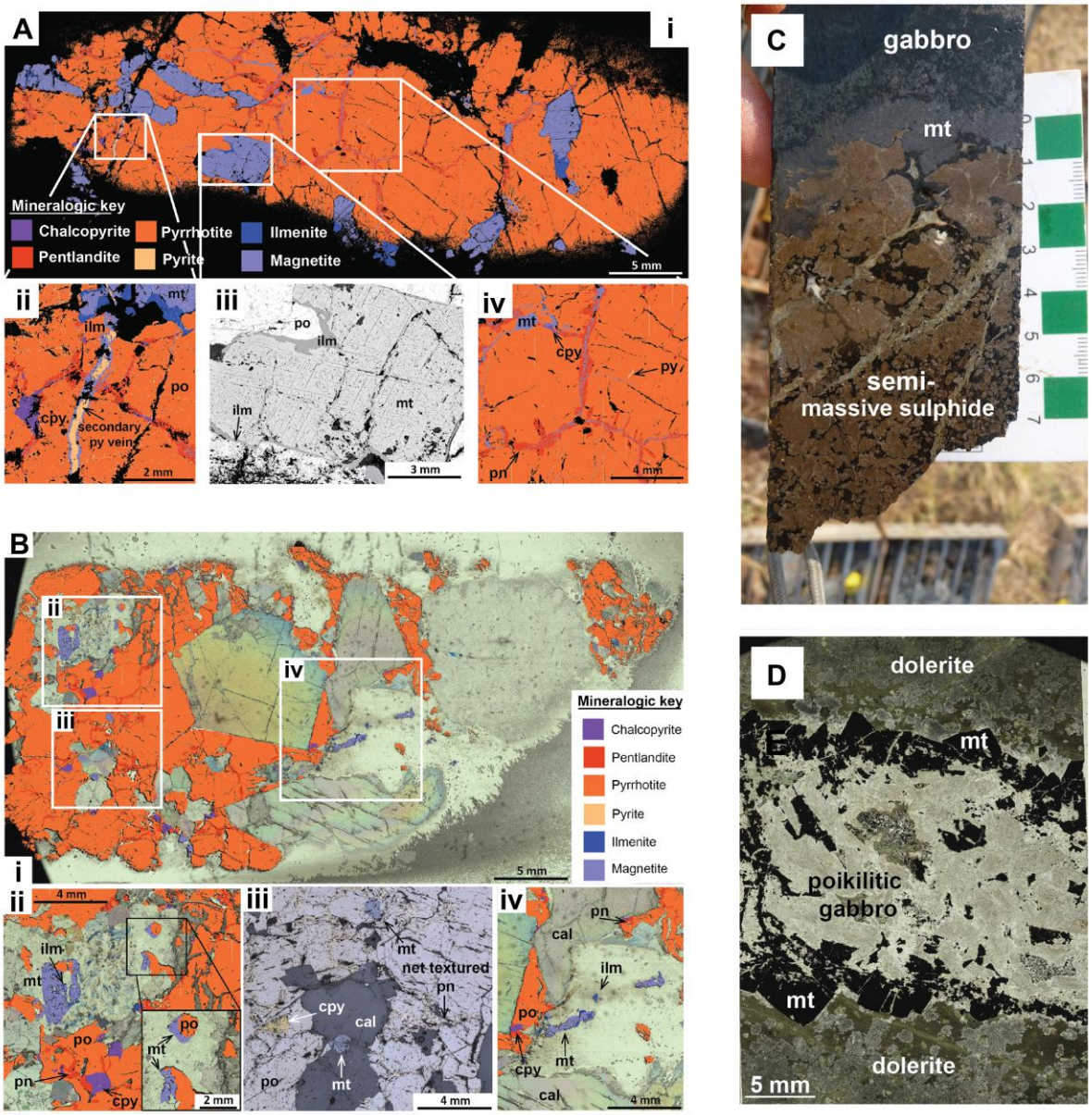
A
i
Mineralogic key
Chalcopyrite
Pyrrhotite
Ilmenite
Pentlandite
Pyrite
Magnetite
5 mm
ii
mt
ilm
po
cpy
secondary py vein
2 mm
iii
po
ilm
ilm
mt
3 mm
iv
mt
cpy
py
pn
4 mm
C
gabbro
mt
semi-massive sulphide
B
ii
iv
iii
i
Mineralogic key
Chalcopyrite
Pentlandite
Pyrrhotite
Pyrite
Ilmenite
Magnetite
5 mm
ii
4 mm
ilm
mt
po
pn
cpy
po
mt
2 mm
iii
mt
net textured
pn
cpy
cal
po
mt
4 mm
iv
pn
cal
ilm
po
cpy
mt
cal
4 mm
D
dolerite
mt
poikilitic gabbro
mt
dolerite
5 mm

Fig 4

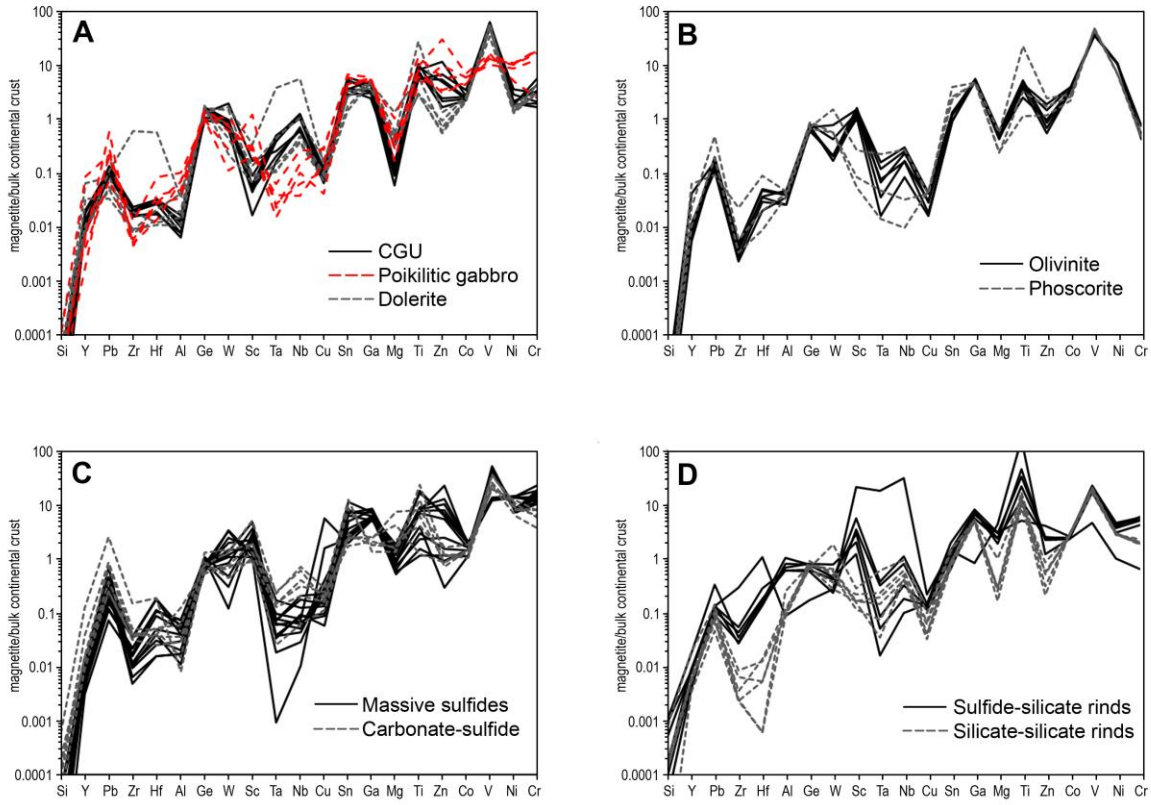
A
B
C
D
magnetite/bulk continental crust
100
10
1
0.1
0.01
0.001
0.0001
Si Y Pb Zr Hf Al Ge W Sc Ta Nb Cu Sn Ga Mg Ti Zn Co V Ni Cr
CGU
Poikilitic gabbro
Dolerite
Olivinite
Phoscorite
Massive sulfides
Carbonate-sulfide
Sulfide-silicate rinds
Silicate-silicate rinds

Fig 5

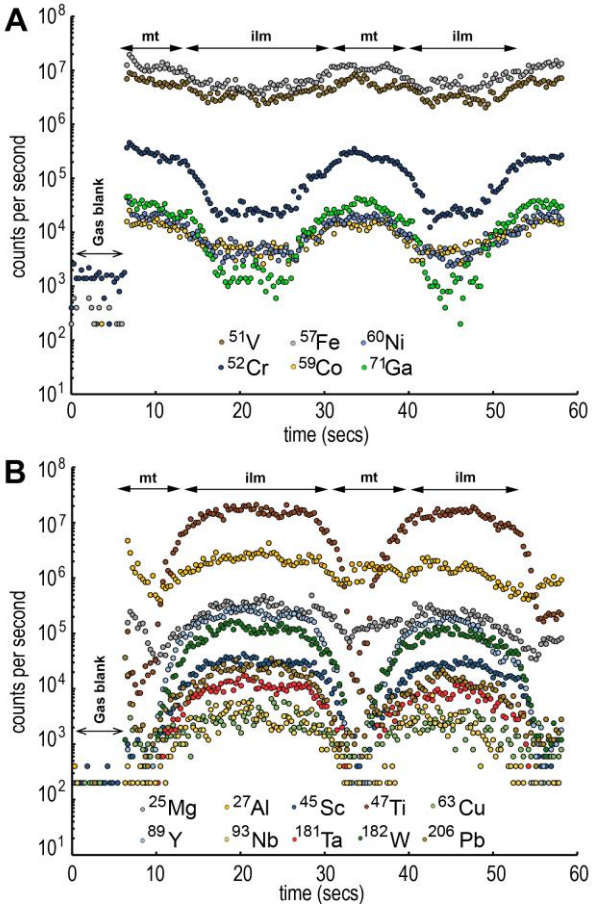
A
mt
ilm
mt
ilm
Gas blank
counts per second
^{51}V
^{57}Fe
^{60}Ni
^{52}Cr
^{59}Co
^{71}Ga
time (secs)
B
mt
ilm
mt
ilm
Gas blank
counts per second
^{25}Mg
^{27}Al
^{45}Sc
^{47}Ti
^{63}Cu
^{89}Y
^{93}Nb
^{181}Ta
^{182}W
^{206}Pb
time (secs)

Fig 6

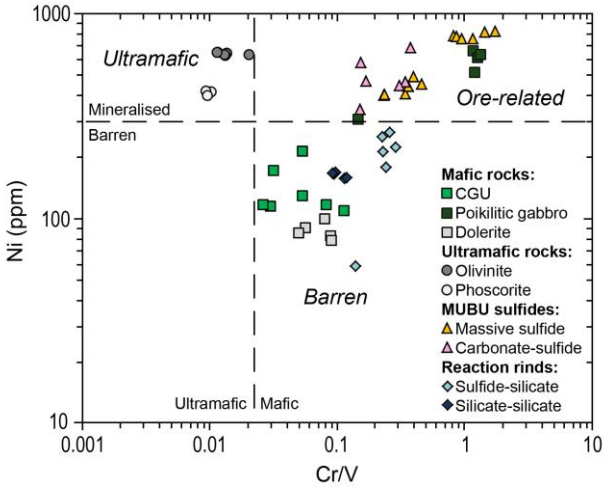
1000
100
10
Ni (ppm)
0.001
0.01
0.1
1
10
Cr/V
Ultramafic
Mineralised
Barren
Ore-related
Barren
Ultramafic
Mafic
Mafic rocks:
CGU
Poikilitic gabbro
Dolerite
Ultramafic rocks:
Olivinite
Phoscorite
MUBU sulfides:
Massive sulfide
Carbonate-sulfide
Reaction rinds:
Sulfide-silicate
Silicate-silicate

Fig 7

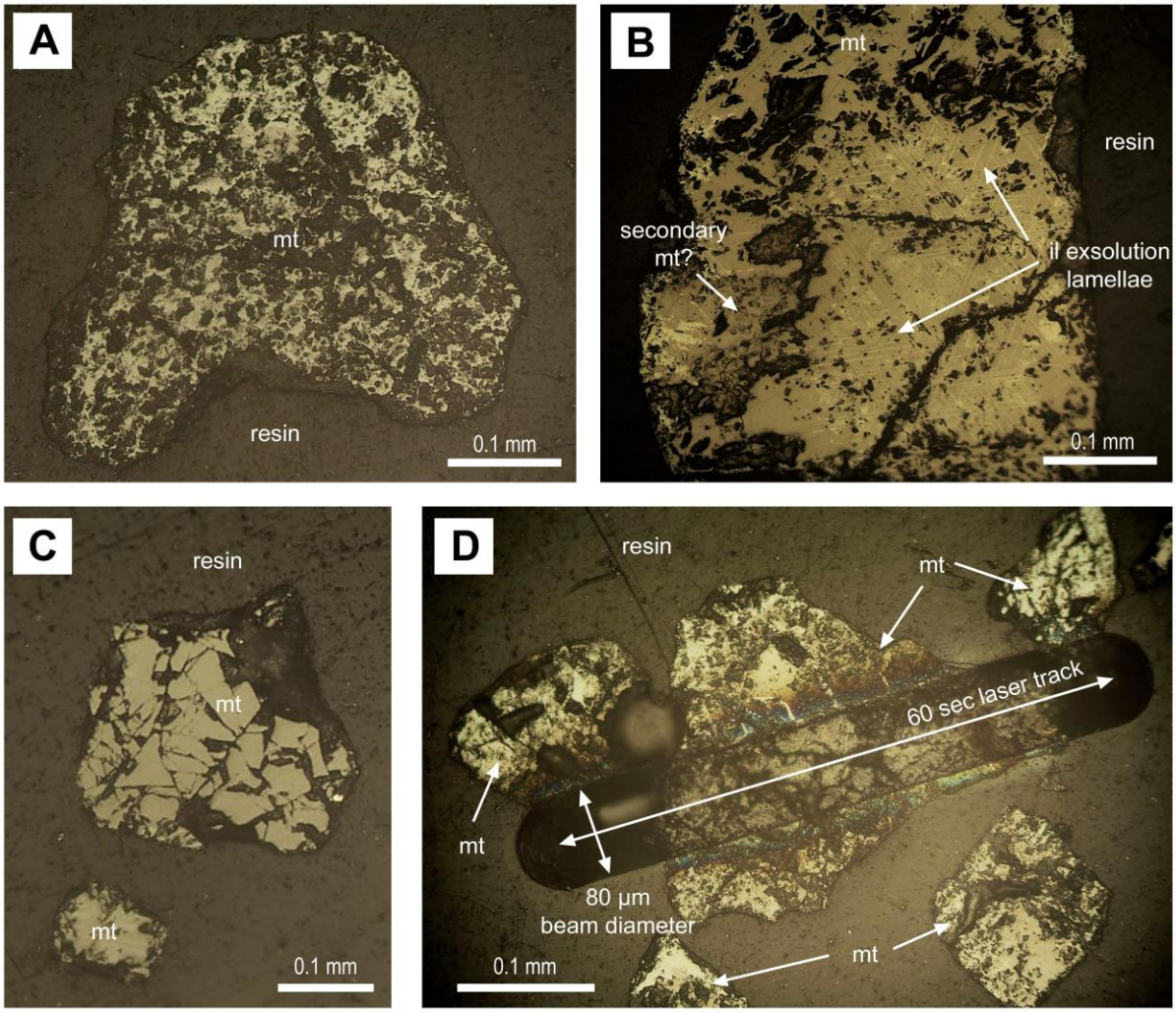
A
mt
resin
0.1 mm
B
mt
resin
secondary
mt?
il exsolution
lamellae
0.1 mm
C
resin
mt
mt
0.1 mm
D
resin
mt
60 sec laser track
mt
80 µm
beam diameter
mt
0.1 mm

Fig 8

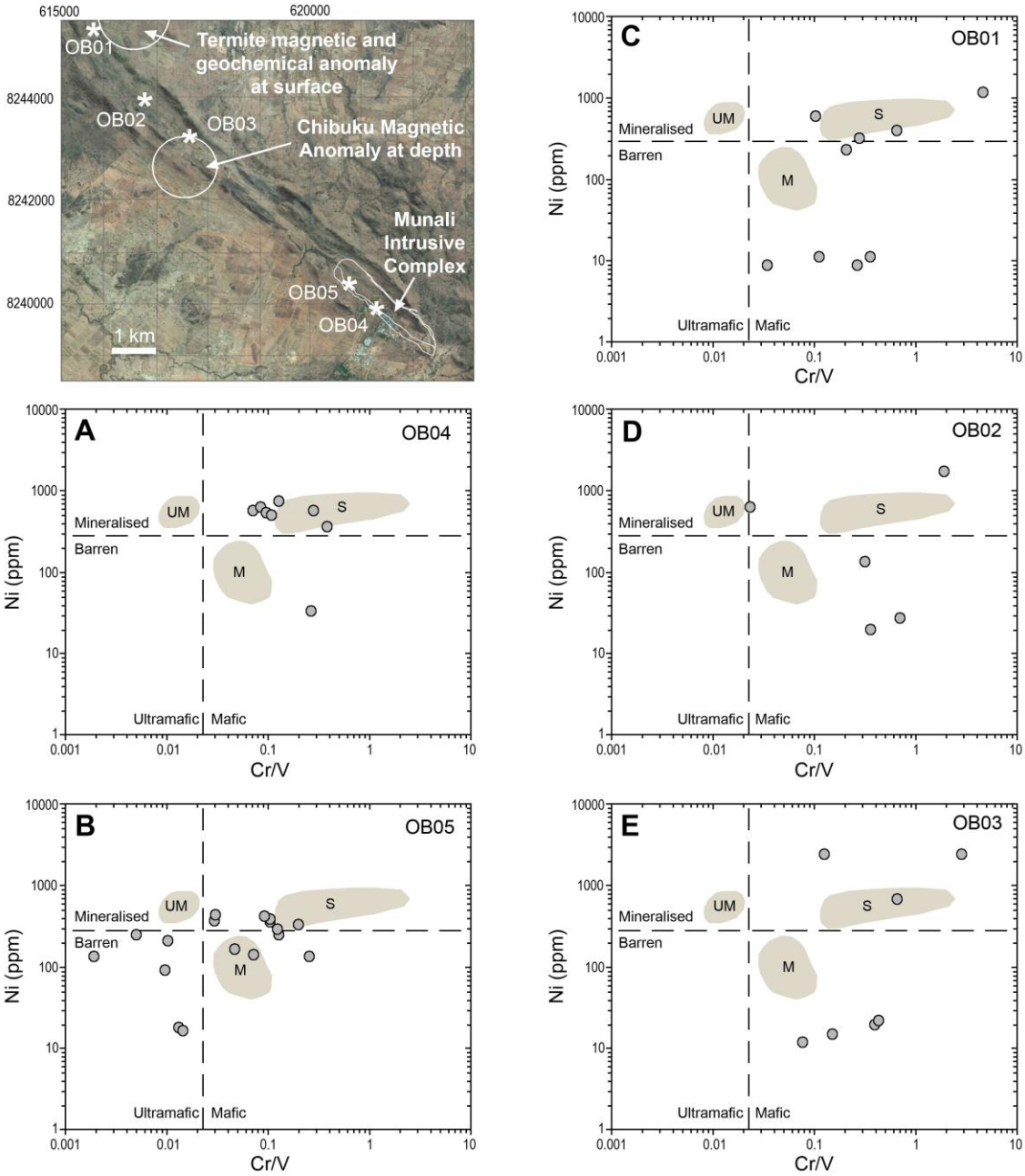
615000
620000
8244000
8242000
8240000
OB01
OB02
OB03
OB04
OB05
Termite magnetic and geochemical anomaly at surface
Chibuku Magnetic Anomaly at depth
Munali Intrusive Complex
1 km
A
B
C
D
E
Mineralised
Barren
Ultramafic
Mafic
UM
M
S
Ni (ppm)
Cr/V

Fig 9

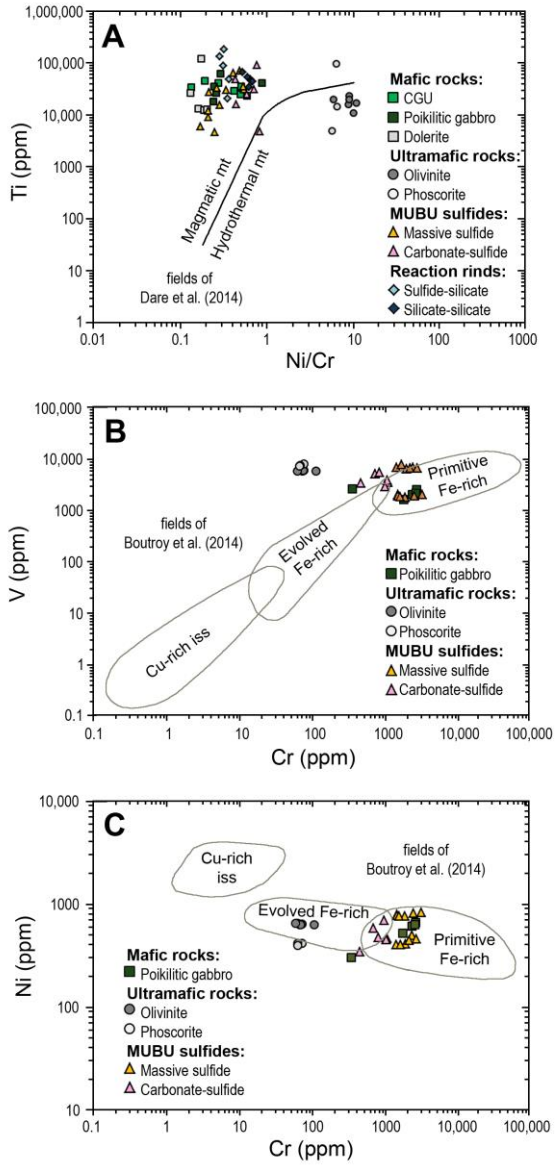
A
Ti (ppm)
Ni/Cr
Magmatic mt
Hydrothermal mt
fields of
Dare et al. (2014)
Mafic rocks:
CGU
Poikilitic gabbro
Dolerite
Ultramafic rocks:
Olivinite
Phoscorite
MUBU sulfides:
Massive sulfide
Carbonate-sulfide
Reaction rinds:
Sulfide-silicate
Silicate-silicate
B
V (ppm)
Cr (ppm)
fields of
Boutroy et al. (2014)
Primitive
Fe-rich
Evolved
Fe-rich
Cu-rich iss
Mafic rocks:
Poikilitic gabbro
Ultramafic rocks:
Olivinite
Phoscorite
MUBU sulfides:
Massive sulfide
Carbonate-sulfide
C
Ni (ppm)
Cr (ppm)
Cu-rich
iss
fields of
Boutroy et al. (2014)
Evolved Fe-rich
Primitive
Fe-rich
Mafic rocks:
Poikilitic gabbro
Ultramafic rocks:
Olivinite
Phoscorite
MUBU sulfides:
Massive sulfide
Carbonate-sulfide

Supplementary data A1: SEM and LA-ICP-MS analytical methodology

SEM analysis

Second generation automated mineralogy was conducted at ZEISS' Natural Resources Laboratory in Cambridge, UK, where Mineralogic Mining software was used to quantitatively classify mineralogy, major element chemistry and magnetite textures through quantitative EDX mapping and spot analysis for stoichiometric collection for LA-ICP-MS normalisation (e.g. Holwell et al., 2017b). A ZEISS Sigma 300 field emission gun Scanning Electron Microscope (SEM) was used, with GEMINI column electron optics, coupled with two Solid State Drift (SSD) Bruker 6 | 30 Energy Dispersive X-ray (EDX) Spectroscopy detectors. Counts for EDX detection were consistently above 3000 (in accordance with ZEISS' QA/QC) with mineral classifications based on stoichiometric values (wt.%). The analyses where taken at 10 µm steps where at each analysis point an EDX spectrum is acquired, has a peak deconvolution, PB-ZAF matrix correction and full spectrum chemical quantification applied, giving the wt% contribution of the elements present for each analysed pixel. These quantified compositions with the chemical data are then passed through a mineral list to classify the analysed locations using a best match method. Standardless Energy-dispersive X-ray spectroscopy calibrations were performed every hour on a Cu standard to perform an EDX energy calibration to the Cu Kα (8.040). Brightness and contrast calibrations were undertaken every 60 minutes to remove any brightness and contrast drift from the Back Scatter Detector (BSD). Analytical operating conditions of 25 keV, using the 60 µm aperture, with the high current mode provided a measured I Probe of 2.6 nA with an analytical working distance of 8.5 mm. Large area photomicrographs were created using the ZEISS Imager Z2M microscope with a motorized 130x85 STEP scanning stage for all seventeen samples (RL and TL). Images were captured with a high resolution AxioCamMR3.

Thin section photomicrographs and Mineralogic maps were layered and visualised using the ZEISS Atlas correlative software.

LA-ICP-MS analysis

Data reduction

Reduction of magnetite standard data was carried out using Iolite. Data reduction for samples of unknown concentrations was conducted offline using Excel. In both cases, ^{57}Fe values collected from quantitative EDX analysis were used as the normalisation element to ensure internal data consistency. Stages to offline data processing were: (1) blank correction; (2) internal normalisation using an internal reference isotope to correct for variations in the efficiency of the laser-ablation process (based on ^{57}Fe Bushveld magnetite standard averaged measured laser concentrations), and (3) a concentration calculation and conversion to ppm. Corrections (calculated using measured concentrations from the magnetite standard BC-28) were applied to account for variations in the tuning and instrument readings on a daily basis, in addition to correcting for the consistent overestimation of isotope concentrations induced by standardising with a high abundance element (^{57}Fe).

Offline data processing for LA-ICP-MS data, in Excel

The Thermo Fisher Qtegra software (software used to collect data analysis) outputs raw data as either an accumulated intensity per element (for the entire region of interest; this was modified based on grain size if grains were too small for a 60 second analysis), or an average intensity per element for the region of interest, or as the intensity per sweep during analyses. There are four stages to processing laser data offline:

Stage 1 – Blank correction. Raw counts per second (cps) intensity data are initially corrected for an average gas blank by subtraction. In addition, five second gas blanks were left at the start of the analysis to correct for background interference and false readings (readings which are similar/the same during gas blank and when the laser is switched on) though were removed during data reduction.

Stages 2 and 3 – Internal normalisation. It is necessary to use an internal reference isotope standard to correct for variations in the efficiency of the laser ablation process (magnetite standard from the Bushveld Complex), and for any matrix effects induced by variations in the type and quantity of the material entering the plasma torch. Prior to LA-ICP-MS analysis, it is therefore necessary to know the accurate content of normalisation elements. ^{57}Fe was used as the normalisation element based on EDX stoichiometric data for samples collected using ZEISS' Mineralogic software. As normalisation values will vary from sample to sample, it is necessary to normalise samples to separate values. Internal normalisation was calculated using equation 1, though note at this stage, only reference isotopes are effected.

Equation 1.

Normalised ^{57}Fe intensities =

Average magnetite standard gas blank corrected ^{57}Fe intensities

x

(^{57}Fe values for mt standard/^{57}Fe stoichiometric value for sample)

As the ablation process affects different samples differently, a further normalisation, or standardisation, corrects all of the intensity data to the same intensity of ^{57}Fe. Using the magnetite standard the calculation is given in equation 2.

Equation 2.

Corrected intensity of any other element =

Normalised intensities for ^{57}Fe in sample

x

(^{57}Fe average values for mt standard gas blank corrected/normalised ^{57}Fe intensities for a sample)

Note that errors in the values for the internal reference isotope (^{57}Fe) will affect the quality of the final data.

<u>Stage 4</u> – Concentration calculation. Calculation of the element concentrations. Magnetite standard values are used to construct the element calibration lines, and the line is fitted through the zero intercept. Concentrations are reported in ppm.

Equation 3.

Concentration of any element =

Intensities of individual element in sample (from stages 2 and 3)

x

(Mt standard acceptance values for that element/Average measured mt standard value for element)

Correction of isotope overestimations

Following data normalisation and conversion of intensities into ppm, a correction value is applied. Using an element in high abundance for data normalisation (^{57}Fe) leads to a consistent overestimation of isotope concentrations, resulting in poor data accuracy. To improve this, isotope estimations were corrected using known measured magnetite standard values in conjunction with magnetite standard acceptance values. Note, data corrections were calculated for each isotope per-day of analysis to account for variation in instrument tuning.

A correction factor for each isotope was calculated using the following equation:

Correction factor =

Certified magnetite standard value/Average measured magnetite standard value

Once a correction value was calculated, the following equation was used to correct LA-ICP-MS ppm data:

Corrected concentrations =

Correction factor for isotope/value (ppm) for element in sample

Data accuracy

Overestimations were corrected using magnetite standard measured values, though as a result initial measures of accuracy are no longer representative. Instead, percentage errors (calculated from magnetite standard 2σ values in Iolite; Table 4) are presented. Importantly, this study aims to find comparative differences between magnetite-style chemistry, and as such, poor data accuracy as a result of isotope overestimation does not impact data interpretation given the applied corrections, high degrees of elemental precision (for critical elements; Ni, V and Cr) and acceptable percentage errors. Isotopes which yield the best percentage error and precision were selected for use.

Technique development and data uncertainty

Instrument calibration is a restrictive factor in obtaining quantitative data. Whilst a methodology established by Dare et al., (2014) was followed, various problems were encountered during both analysis and data reduction. Typically during LA-ICP-MS analysis, a certified reference material is used (e.g. NIST glass) for laser calibration. However, in the case of this study, an external reference material (natural magnetite standard) was used for several reasons: (1) NIST is a glass and as such, behaves differently to magnetite during the

ablation process and (2) calibrations using NIST relies on Si values as the normalisation element, which is not possible for magnetite given low Si abundances.

Laser spots were insufficient in acquiring data for all elements based on data collection time, often appearing below detection. This issue was resolved using laser tracks, though added a constraint to the smallest grains that could be analysed. It is important to note that whilst laser tracks ablate the surface of grains; it is unknown what material lies underneath and may potentially introduce erroneous readings.

[57]Iron values were used as the normalisation element as it was the only element consistently detected during EDX analysis. As discussed, high element concentrations introduce problems during data reduction. Using a different technique to collect normalising values (e.g. electron microprobe as opposed to EDX values) in lower abundances is recommended for use in further analytical work, though crucially, elements valuable for data interpretation cannot be used as they are needed for data reduction.

Supplementary data A2

	All values in ppm																				
	25Mg	27Al	29Si	45Sc	47Ti	51V	52Cr	59Co	60Ni	63Cu	66Zn	71Ga	74Ge	89Y	90Zr	93Nb	118Sn	178Hf	181Ta	182W	206Pb
Limits of detection	0.53	0.25	1	0.15	0.53	0.06	0.5	0.05	0.2	0.15	0.34	0.03	0.22	0.0055	0.01	0.0024	0.1	0.0074	0.005	0.01	0.04
Lithology																					
Mafic rocks	25Mg	27Al	29Si	45Sc	47Ti	51V	52Cr	59Co	60Ni	63Cu	66Zn	71Ga	74Ge	89Y	90Zr	93Nb	118Sn	178Hf	181Ta	182W	206Pb
CGU																					
M349.5_1	3306.22	3624.42	9.12	1.16	34567.61	7570.07	411.89	72.34	211.43	3.39	845.47	73.52	2.18	0.26	2.81	9.32	10.20	0.12	0.34	0.97	1.51
M349.5_2	4154.63	2392.56	18.08	1.38	33169.93	6963.10	795.63	59.97	109.06	2.21	123.46	39.96	1.42	0.36	2.62	8.42	5.91	0.10	0.36	0.98	1.41
M349.5_3	9474.44	5091.35	52.03	0.98	44237.16	7155.65	595.63	64.55	116.21	2.36	154.81	49.27	1.24	0.40	3.18	9.71	4.94	0.12	0.27	0.85	1.33
M349.5_4	1716.03	1952.99	-10.75	0.37	28645.36	8717.96	264.94	70.17	114.01	2.00	180.27	51.89	1.94	0.15	2.09	5.71	6.38	0.07	0.11	0.68	1.00
M349.5_5	2641.75	2345.76	-9.03	1.07	24094.11	8544.06	228.10	68.29	116.30	1.79	394.81	52.98	2.08	0.20	2.22	5.00	9.38	0.06	0.14	0.90	1.22
M349.5_6	4529.70	4110.05	7.73	3.79	22933.05	8787.06	283.20	93.52	170.57	2.22	488.97	82.17	1.68	0.22	2.52	4.81	6.22	0.11	0.18	1.99	1.29
M349.5_7	2566.16	3010.06	1.43	1.99	39646.96	8310.57	452.54	63.98	128.00	2.71	353.80	69.89	1.84	0.25	2.41	10.23	8.59	0.13	0.32	0.88	1.46
*Poikilitic gabbro**																					
M302.8_1	17098.35	6150.37	43.15	2.05	12657.27	7420.30	604.69	70.13	99.43	2.77	68.26	83.25	2.11	1.24	1.04	3.91	4.46	0.05	0.07	1.50	0.95
M302.8_2	37745.46	10591.68	88.09	2.98	26036.61	6806.43	613.74	62.36	81.41	4.82	50.92	73.71	1.66	0.16	81.52	8.78	4.48	2.13	0.33	0.80	1.25
M302.8_3	10529.09	4529.89	33.16	1.51	12029.99	8203.09	466.70	63.25	89.80	2.48	44.46	76.20	2.37	0.17	2.51	3.10	2.92	0.05	0.10	0.22	0.63
M302.8_4	8688.75	3203.68	17.86	1.88	12576.69	8042.47	408.94	57.84	84.18	1.97	40.17	76.58	2.07	0.65	1.21	2.92	2.44	0.04	0.08	0.45	0.37
M302.8_5	13821.67	12636.99	226.23	7.56	117193.07	4777.29	434.53	66.90	77.74	4.14	98.26	59.02	1.74	0.21	1.19	45.88	5.82	0.08	2.71	1.67	0.54
Dolerite																					
090-338.2_1	8581.74	14956.43	31.18	5.22	40861.63	2279.36	338.42	188.62	302.66	7.35	2162.87	95.97	2.00	0.12	0.58	2.17	11.64	0.15	0.04	0.78	6.56
090_338.2_2	4805.36	10439.20	-2.58	7.00	34430.10	2176.17	2598.57	121.74	653.86	1.15	223.40	93.45	1.75	0.08	0.62	0.83	7.73	0.10	0.01	0.61	0.85
090_338.2_3	29881.64	31406.07	155.80	26.93	59937.51	1415.80	1733.01	158.71	514.95	8.28	429.38	78.38	1.27	1.66	1.74	1.20	10.11	0.31	0.02	0.28	2.46
090_338.2_4	12684.80	21202.00	39.23	5.77	25938.16	1780.84	2300.87	126.47	606.88	2.98	253.60	88.88	1.29	0.14	0.78	0.51	7.07	0.11	0.02	1.11	2.29
090-338.2_5	8312.33	22019.30	21.77	4.74	17646.41	1864.52	2534.40	162.75	626.58	4.16	712.10	93.67	1.32	0.04	0.65	0.31	7.60	0.05	0.03	0.11	3.18
Ultramafic rocks	25Mg	27Al	29Si	45Sc	47Ti	51V	52Cr	59Co	60Ni	63Cu	66Zn	71Ga	74Ge	89Y	90Zr	93Nb	118Sn	178Hf	181Ta	182W	206Pb
*Olivinite**																					
M292.6_1	12133.27	7882.80	8.05	25.89	15591.92	5144.56	70.92	88.92	639.22	0.49	39.78	81.00	1.00	0.23	0.38	1.32	1.58	0.11	0.05	0.17	1.35
M292.6_2	13230.28	10815.82	4.93	22.90	10590.08	5328.62	62.35	97.24	644.87	0.44	70.07	88.83	0.94	0.20	0.30	0.67	1.59	0.07	0.01	0.21	1.20
M292.6_3	13322.98	7882.47	14.09	30.83	19385.04	5013.87	103.49	94.29	628.61	0.79	50.16	81.58	0.84	0.13	0.54	2.05	1.99	0.13	0.08	0.21	1.64
M292.6_4	16895.37	11733.42	20.40	33.43	22407.03	5039.18	67.17	93.78	621.76	1.17	62.02	85.36	0.93	0.17	0.66	2.40	2.31	0.18	0.11	0.79	2.17
M292.6_5	16699.07	12435.97	19.06	36.18	19220.81	5221.98	68.67	106.52	627.63	1.14	137.35	88.17	0.79	0.81	0.65	1.87	2.18	0.19	0.05	0.21	1.79
M292.6_6	16242.35	14222.69	1.36	29.70	16458.99	5000.55	57.92	104.33	643.77	0.83	106.94	90.15	1.05	0.11	0.49	1.38	2.15	0.14	0.03	0.43	1.89
*Phoscorite**																					
036-215-5_1	7088.84	11087.00	3.17	1.20	4787.90	6851.32	71.40	59.17	412.89	1.29	86.52	77.03	0.88	0.20	0.45	0.08	3.94	0.03	0.01	0.57	2.12
036-215-5_2	6969.66	12787.74	4.28	1.87	13987.42	6622.00	62.65	69.54	416.14	1.15	123.84	75.64	1.15	0.45	0.78	0.26	4.44	0.08	0.03	0.56	5.40
036-215-5_3	16137.84	14110.24	3.59	5.77	95298.25	6339.95	61.60	78.05	397.17	1.11	180.42	76.06	0.94	1.19	3.06	2.21	6.87	0.33	0.16	1.53	1.02
Massive sulfides*	25Mg	27Al	29Si	45Sc	47Ti	51V	52Cr	59Co	60Ni	63Cu	66Zn	71Ga	74Ge	89Y	90Zr	93Nb	118Sn	178Hf	181Ta	182W	206Pb
M332.0_1	48971.93	15596.89	7.66	75.91	65030.42	1556.36	1831.47	47.61	755.20	3.72	464.12	94.17	0.78	0.10	4.52	1.36	12.72	0.64	0.05	0.79	1.55
M332.0_2	40739.74	17031.81	-2.31	61.97	32936.52	1780.74	3132.74	49.72	821.91	2.28	694.75	108.79	1.11	0.08	2.78	0.54	11.30	0.40	0.04	0.28	1.17
M332.0_3	41932.73	20684.56	9.45	42.24	30314.14	1653.09	2416.64	44.06	813.12	4.73	1544.12	77.41	0.91	0.09	2.19	0.47	10.27	0.38	0.05	1.12	1.90
M332.0_4	25588.34	14324.96	0.30	52.85	30765.80	1749.90	1439.72	48.99	784.06	1.51	547.36	120.34	1.32	0.06	1.98	0.71	8.05	0.30	0.02	0.45	0.77
M332.0_5	31974.21	21279.49	2.00	59.47	35631.23	1645.23	1434.90	51.55	775.23	2.50	879.75	130.31	1.26	0.11	2.72	0.64	11.36	0.37	0.03	0.12	1.27
M332.0_6	31805.68	11125.81	13.27	98.68	71270.06	1610.23	1540.72	48.47	756.03	5.84	417.12	109.24	1.06	0.23	4.18	1.55	17.92	0.63	0.05	1.29	4.83
020-311-3_1	19833.68	8401.39	3.44	29.53	9172.28	5840.29	2331.71	40.64	491.67	7.09	165.97	92.12	0.79	0.15	1.18	0.22	4.07	0.09	0.01	1.42	4.21
020-311-3_2	14022.54	4892.65	13.56	24.26	6093.54	5793.47	2679.89	37.06	455.92	10.25	62.16	91.03	0.77	0.10	0.82	0.38	4.64	0.06	0.04	3.16	2.52
020-311-3_3	22623.09	11422.69	2.68	45.95	27799.34	5525.35	1912.45	39.54	406.54	3.45	370.00	96.51	0.84	0.17	1.49	0.93	4.66	0.17	0.11	1.89	2.58
020-311-3_4	23940.84	3223.82	57.99	19.42	15617.41	5933.18	1394.64	28.56	399.20	143.39	19.88	79.51	0.97	0.07	1.28	0.59	3.21	0.14	0.06	3.07	2.51
020-311-3_5	16709.25	5781.67	60.80	31.53	11961.86	5811.99	2111.68	35.77	443.17	7.87	104.70	89.98	0.72	0.21	1.39	0.33	5.87	0.11	0.02	2.34	7.13
020-311-3_6	15559.10	4881.73	16.21	22.13	4628.34	6740.02	1602.94	28.04	403.44	40.18	79.31	86.31	0.89	0.13	0.62	0.08	3.89	0.05	0.00	1.02	3.02
Carbonate-sulfide vei	25Mg	27Al	29Si	45Sc	47Ti	51V	52Cr	59Co	60Ni	63Cu	66Zn	71Ga	74Ge	89Y	90Zr	93Nb	118Sn	178Hf	181Ta	182W	206Pb
M326.8_1	113073.30	16904.10	186.27	22.02	4854.69	4446.33	688.54	36.97	577.13	2.86	59.76	38.01	1.07	0.28	4.42	0.47	3.94	0.18	0.02	0.42	2.51
M326.8_2	41762.57	8152.66	53.02	27.07	24941.56	4724.55	801.27	34.80	469.62	6.30	59.72	31.68	0.69	0.17	3.92	2.37	2.81	0.09	0.10	0.63	2.60
M326.8_3	59341.93	10157.83	112.48	18.56	16217.82	3050.40	1058.86	30.94	465.48	4.07	80.18	27.59	0.67	0.29	4.89	1.58	4.57	0.13	0.09	0.69	7.42
M326.8_4	44867.41	4198.45	116.11	38.20	49224.17	3321.98	1032.44	36.76	445.73	4.31	48.09	27.18	1.59	0.68	6.50	4.59	14.28	0.17	0.16	1.40	9.09
M326.8_5	198737.78	35408.11	271.37	40.77	31181.51	2525.23	957.99	46.92	683.45	5.32	109.96	35.99	0.80	0.24	5.28	3.08	3.82	0.13	0.10	0.71	3.95
M326.8_6	36573.93	2335.28	746.13	104.51	92852.75	2905.30	444.96	26.29	341.38	7.33	78.40	20.24	0.94	2.24	18.83	5.36	19.88	0.65	0.15	1.28	26.83
Reaction rims	25Mg	27Al	29Si	45Sc	47Ti	51V	52Cr	59Co	60Ni	63Cu	66Zn	71Ga	74Ge	89Y	90Zr	93Nb	118Sn	178Hf	181Ta	182W	206Pb
*Sulfide-silicate**																					
20-332_1	64580.99	205052.58	686.89	42.62	48363.58	3023.22	689.38	62.44	250.81	3.67	171.85	114.26	1.03	0.15	3.53	1.43	2.34	0.52	0.04	0.76	1.54
20-332_2	118535.53	26392.26	50.62	449.42	636310.15	610.16	85.84	60.07	58.55	5.77	84.51	13.08	0.22	0.07	38.04	238.73	2.40	3.93	12.16	0.27	1.43
20-332_3	80505.84	180157.89	1260.73	73.91	132329.76	2663.22	775.57	62.21	223.06	2.98	177.81	102.26	0.76	0.15	5.70	6.39	1.08	0.67	0.22	0.23	1.19
20-332_4	85334.51	300291.65	1457.56	26.43	20761.96	2861.33	750.81	68.43	264.00	3.83	288.06	125.08	0.98	0.32	4.53	0.78	3.21	0.60	0.01	0.45	3.53
20-332_5	65664.16	177530.67	215.15	118.93	182133.23	2279.52	557.95	60.18	177.89	3.86	157.62	87.81	0.80	0.17	7.02	8.55	2.05	1.02	0.26	0.41	1.45
20-332_6	52949.54	235309.99	129.03	62.92	89370.63	2887.81	670.55	59.04	211.91	3.53	167.85	117.08	1.00	0.09	3.75	2.50	1.68	0.51	0.06	0.45	0.99
Silicate-silicate																					
63-208B_1	8232.68	34617.23	237.31	3.51	33919.42	2748.19	268.15	68.40	167.31	1.63	40.72	81.61	0.90	0.10	0.48	3.17	1.49	0.05	0.10	0.27	0.96
63-208B_2	7786.15	25350.86	254.72	6.12	67671.16	2608.90	300.48	69.44	157.54	2.68	36.32	78.49	0.84	0.11	1.15	7.48	2.44	0.05	0.42	1.78	1.15
63-208B_3	6893.75	28406.59	175.11	4.71	48002.89	2696.09	255.87	66.03	164.61	1.79	39.28	81.27	0.86	0.10	0.87	4.79	2.31	0.02	0.16	0.36	0.71
63-208B_4	27924.42	74797.32	1077.36	3.52	54156.58	2169.34	261.22	67.42	158.12	1.14	21.97	77.03	0.97	0.34	0.34	3.94	1.42	0.00	0.13	0.63	1.49
63-208B_5	4570.14	25169.61	2.44	2.51	44718.27	2565.79	250.90	71.56	168.34	0.89	15.09	76.94	1.15	0.06	0.31	3.38	1.14	0.00	0.05	0.49	0.50
63-208B_6	7977.50	32496.65	187.28	3.36	44607.95	2594.72	241.35	69.99	166.91	1.07	59.59	74.86	0.96	0.11	0.31	3.18	1.42	0.02	0.02	0.58	0.80
* = contains sulfide																					
Soil samples	25Mg	27Al	29Si	45Sc	47Ti	51V	52Cr	59Co	60Ni	63Cu	66Zn	71Ga	74Ge	89Y	90Zr	93Nb	118Sn	178Hf	181Ta	182W	206Pb
OB 01																					
OB 1_image 2_point 5&4_	590.230316	523.0495735	10.6405	0.383	416.9601493	11.337155	8.1328082	1927.1744	45240.641	11.8792	10.4766	0.1697	0.02593	0.01414	2.95886	0.27885	2.58361	0.05957	0.02493	0.20494	31.1961
OB 1_6_85um	249.228317	1923.088085	-14.582	24.3834	16014.02749	319.96921	10.730821	7.7378469	8.8791904	3.38325	13.2601	8.7809	0.39466	0.13828	2.46244	16.0567	49.4201	0.09158	3.18031	12.7097	30.081
OB 1_2_85um3mJ	195.381792	1810.342763	18.18104	0.67219	522.6704973	1044.18521	686.33472	23.92757	405.29579	1.32351	8.11486	23.0752	2.11647	0.00986	1.44652	0.21967	2.25256	0.0258	0	0.39859	4.86233
OB 1_image1_point 4_85u	646.308603	1835.166008	15.1181	25.1007	33259.86069	581.410288	211.23694	2.8133888	10.974855	6.51426	12.1838	9.15537	0.92027	1.26524	80.6567	46.6866	82.7511	2.95015	7.20586	6.24734	15.3343
OB 1_Image 5_point2_85u	401.51719	3075.680838	77.92471	27.6512	15968.80239	328.505021	36.944185	9.8688122	11.411806	15.6833	10.9345	8.53096	0.64162	0.48206	5.5521	12.9026	50.3754	0.18498	2.83836	27.7315	54.1576
OB 1_image 1_point 6_85	487.245441	2078.994134	6.339132	26.9108	21509.30512	365.656896	144.76061	17.017626	20.947322	23.3327	15.5104	12.5997	0.49005	0.57054	6.54494	17.3057	42.5468	0.19087	3.19144	2.76041	76.7414
OB 1_3_85um_3mJ	3301.15092	14538.48469	368.7117	40.4786	1824.663705	808.365661	3856.9666	380.27263	1182.9085	2013.49	34.7152	82.5409	3.18664	11.5372	104.202	10.8523	2.86446	1.8811	0.06531	11.3784	976.916
OB 1_4_85um	218.957791	1518.688144	0.63535	21.987	12710.59747	297.707815	79.924473	2.8540471	8.7313489	52.4183	12.072	11.1554	0.77161	0.09933	6.32834	54.1362	58.0367	0.17656	4.64792	1.93997	8.23433
OB 1_5_85um	6595.12662	12342.27077	470.7239	27.8619	1600.048081	1160.42951	236.55047	276.45507	243.42058	64.847	226.387	57.8017	2.69122	15.7106	70.9403	2.5332	5.55847	1.58984	0.22389	8.71809	1162.73
OB 1_7_85um	8748.19552	15300.54554	598.0741	31.3215	386.0699974	607.053445	61.161869	2468.4203	609.43705	120.12	28.0034	25.9568	8.43017	20.6144	89.434	1.08779	1.61113	1.83503	0.23994	72.7246	2809.22
OB 1_8_85um	8856.30958	16329.68172	637.4975	30.6522	390.4027416	507.915297	143.83035	861.99642	330.53369	151.612	32.7856	26.2387	7.59344	16.6397	607.383	1.71789	1.98442	7.39595	0.27599	88.3836	3847.94
OB 02																					
OB 2_image 2_point1-4_8	1862.65548	8377.996555	526.5862	6.70181	1242.446678	725.563338	237.46535	151.68235	130.52733	12.5691	42.5187	15.0616	14.5019	5.96671	94.8754	7.56606	6.16697	2.46091	0.19637	2575.19	265.582
OB_2_image1_point1-3_8	10985.5034	9186.702039	178.0833	14.4637	2197.508071	1215.48348	30.719123	10385.084	670.37598	48.3187	38.7503	33.7454	1.18627	14.447	218.712	18.9644	3.76385	7.01345	0.3648	49.4263	185.39
OB_2_1_85um	1976.41215	8887.923119	49.57587	32.5785	64214.06925	1223.81816	866.3941	4.2806063	26.502956	13.3191	24.3375	10.9877	0.19908	8.71926	205.154	168.086	72.2511	6.45334	4.9162	39.5705	7.24562
OB_2_image 9_point 6-8_	6436.40784	17788.97505	206.4358	47.9522	1915.028649	1039.18226	2011.6557	3086.5402	1827.5524	49.1725	65.3345	81.2391	2.99268	44.3841	169.778	1.68506	9.21886	4.11283	0.08863	13.4055	325.343
OB_2_2_85um	763.27956	2347.987821	6.538329	55.4494	58564.68424	1458.11443	563.23702	8.516875	20.367658	0.78013	11.0863	14.8608	0.15638	2.68304	123.568	1.62708	57.8985	4.64081	0.29186	0.3874	5.83978
OB 03																					
OB_3_1_85um	216.275878	380.8474241	1.468792	47.1171	29619.94572	5112.80956	781.46337	1.3921459	15.330843	2.02851	6.66102	9.25687	0.21242	0.09111	1.5489	2.157	254.905	0.08668	0.36031	33.5222	2.43232
OB_3_2_85um	1695.12786	7624.544893	51.99258	47.6896	59141.01862	1566.9807	621.31346	5.0834463	20.62088	8.72371	13.7289	12.5948	0.26715	3.41826	54.1059	6.82565	80.9026	1.6576	0.38248	3.50981	4.45915
OB_3_3_85um	1952.58253	14513.25526	62.58249	118.175	3341.687316	433.127129	275.54223	574.48435	737.78018	12.2189	46.7336	149.931	1.79346	171.632	66.1724	2.24283	8.44267	1.83789	0.19169	3.68973	49.5586
OB_3_4_85um	7383.28973	10786.91742	141.055	18.1086	252.0335841	1389.72744	178.3684	4572.4472	2438.1681	42.2602	40.3046	71.6173	2.27015	17.301	20.5625	0.27231	3.75526	0.54273	0.00566	6.0711	64.4676
OB 3_5_85um	812.58308	4175.938983	37.16575	39.2935	21925.98044	1835.66743	146.27929	7.0503755	11.983693	4.71703	7.90653	18.4108	0.36191	0.37635	4.41215	15.2242	65.1066	0.15084	3.29577	1.28892	2.31472
OB 3_image5_point1_85u	7052.11187	8681.324699	75.82189	41.1595	59433.41849	1512.49824	653.91811	5.7935549	22.99965	13.0101	17.8241	11.3764	0.38266	5.39134	39.4729	20.023	73.4217	0.90528	9.54708	40.7714	10.2668
OB 3_7_85um	2781.46806	15643.96076	99.75653	36.6257	1982.914016	2416.4681	7610.9464	152.51156	2426.8764	68.5558	29.1745	43.1573	4.55648	20.9294	399.689	4.43389	4.28945	5.95732	0.06514	35.2954	65.4261
OB 04																					
OB 4_image8_point1-4_8	1483.93293	5834.354333	46.74109	5.43654	491.7527787	6788.96591	571.45153	83.43106	676.79974	1.97299	25.1494	69.7456	0.60576	1.3907	1.03639	0.03947	2.34309	0.09998	0.00087	0.30479	3.54484
OB 4_image9_point1-3	1146.11367	2344.356261	24.54625	2.07363	6770.282321	6625.45441	456.19919	59.606113	605.82688	0.89686	23.0509	40.2471	0.47542	0.64172	0.38055	0.19582	2.40056	0.0269	0.02365	0.24695	1.89025
OB4_image7_point1-3_85	1529.98988	2060.727248	27.90389	1.47022	6897.132403	2913.33349	309.29993	52.733278	538.55209	1.08681	10.7533	5.39205	0.71908	0.96384	0.99312	0.98156	4.12611	0.06919	0.17076	0.40459	3.40083
OB4_image7_85um	1254.19114	7912.784035	59.25815	4.31438	505.7236492	4741.63955	599.58718	36.648089	769.1677	6.89835	22.5752	44.8457	0.64124	2.79687	1.87303	0.22369	3.53958	0.05405	-0.00057	0.41513	2.85653
OB4_image5_85um	124.940889	612.3022308	4.729242	0.65748	156.7449469	4521.00847	439.94517	33.190111	562.89922	0.33602	8.13184	23.3282	0.3995	0.77678	0.38578	0.05975	0.69563	0.00944	-0.00129	0.9174	1.84737
OB 4_2_85um	127.227084	291.0632622	2.294767	1.5191	266.0249293	4711.01527	1760.2731	57.290555	379.09716	0.64605	11.215	34.9082	0.46511	2.01771	2.72589	0.18809	0.90623	0.20231	-0.00112	0.25452	1.72253
OB4_4_85um	169.112392	934.3412694	1.975809	0.88741	720.5406003	5164.59498	1463.1159	48.057806	619.74185	0.46398	21.7861	27.147	0.20783	0.1782	0.52877	0.30303	2.47387	0.01203	0.02083	0.86467	1.2053
OB 4_3_85um (14-26secs)	735.550498	6119.065474	56.88824	31.6576	26295.79043	547.857666	145.35478	6.4435896	35.544208	2.82245	12.3956	9.9825	0.472	3.36076	6.64397	21.7418	65.0905	0.35167	4.25955	7.21039	6.8581
OB 05																					
OB 5_1_85um (20-50secs)	386.811223	1859.163876	5.925164	3.07733	28010.1574	9621.36646	101.16658	68.335185	227.45306	2.60412	222.299	55.1943	1.53402	0.45354	1.60902	6.86276	1.98608	0.08591	0.38948	0.13573	12.6599
OB 5_3_85um (20-40secs)	1502.51102	24275.41292	146.492	23.7236	2713.835875	3402.17076	691.20391	6.6501877	345.4194	10.4225	22.0968	35.8414	1.03957	2.79282	113.043	0.36542	2.96544	2.59726	0.01068	0.53521	10.2984
OB 5_4_85um (30-44secs)	596.756427	2563.784995	23.4241	3.36867	16829.59611	7520.64576	695.70159	21.90819	443.85787	12.4493	40.3016	51.7801	0.26756	1.18258	5.9193	1.82881	1.21503	0.19951	0.29121	2.79166	8.78084
OB 5_5_85um (20-40secs)	1947.91537	39.14794599	0.56225	26.2091	525625.8722	1320.62118	18.827776	44.032605	17.546135	4.00165	185.476	0.9551	-0.03637	0.02356	3.66572	875.59	19.5682	1.06828	78.4228	0.17387	1.55451
OB 5_6_85um (20-40secs)	1808.38788	271.7059098	1.38586	25.3994	511678.4641	1290.54295	18.682292	51.207954	18.945839	5.65127	194.423	0.76166	0.31578	0.03254	3.00053	866.826	18.266	0.87373	71.9015	0.1513	2.66986
OB 5_7_85um (16-48 secs)	247.614581	1055.605905	3.675466	1.24926	16670.33055	7060.67915	737.04942	47.072076	415.12074	1.54918	51.0582	52.7028	0.71207	0.18492	0.8896	0.68131	1.44388	0.01766	0.02426	0.23173	4.97261
OB 5_8_85um (20-40secs)	407.039886	1990.205021	10.24542	3.1178	34139.43577	6754.56803	684.53082	47.35855	395.90798	2.20274	42.8781	48.5667	0.68916	0.53967	1.10896	1.28602	1.33787	0.03986	0.05176	0.30939	3.53356
OB 5_9_85um (16-50secs)	449.397823	1195.160465	3.879146	1.85713	16249.0719	6522.87477	196.57355	57.819329	481.44067	0.72749	137.057	63.2849	0.42803	0.12098	0.66773	1.61765	0.91358	0.01129	0.13146	0.17756	1.76203

1023